

1       **Observations of relative humidity effects on aerosol light**  
2                   **scattering in the Yangtze River Delta of China**

3  
4       **Zhang Lu<sup>1,2</sup>, Sun Junying<sup>1,3</sup>, Shen Xiaojing<sup>1</sup>, Zhang Yangmei<sup>1</sup>, Che Haochi<sup>1</sup>,**  
5                   **Ma Qianli<sup>4</sup>, Zhang Yiwen<sup>1</sup>, Zhang Xiaoye<sup>1</sup>, John A. Ogren<sup>5</sup>**

6       <sup>1</sup> Key Laboratory of Atmospheric Chemistry of CMA, Institute of Atmospheric  
7       Composition, Chinese Academy of Meteorological Sciences, Beijing 100081, China

8       <sup>2</sup> College of Earth Science, University of Chinese Academy of Sciences, Beijing  
9       100049, China

10       <sup>3</sup> State Key Laboratory of Cryospheric Sciences, Cold and Arid Region  
11       Environmental and Engineering Research Institute, Chinese Academy of Sciences,  
12       Lanzhou 730000, China

13       <sup>4</sup> LinAn Regional Atmosphere Background Station, LinAn 311307, China

14       <sup>5</sup> Earth System Research Laboratory, NOAA, Boulder, CO, USA

15       *Correspondence to:* J.Y. Sun (jysun@cams.cma.gov.cn)

16  
17       **Abstract**

18       Scattering of solar radiation by aerosol particles is highly dependent on relative  
19       humidity (RH) as hygroscopic particles take up water with increasing RH. To achieve  
20       a better understanding of the effect of aerosol hygroscopic growth on light scattering  
21       properties and radiative forcing, the aerosol scattering coefficients at RH in the range  
22       of ~40% to ~90% was measured using the humidification system (consists of two  
23       nephelometers operating in series with a humidifier in between) in the Yangtze River  
24       Delta of China in March 2013. In addition, the aerosol size distribution and chemical  
25       composition were measured. During the observation period, the mean and standard  
26       deviation (SD) of enhancement factors at RH=85% for the scattering coefficient  
27       ( $f(85\%)$ ), backscattering coefficient ( $f_b(85\%)$ ) and hemispheric backscatter fraction  
28       ( $f_{\beta}(85\%)$ ) were  $1.58\pm 0.12$ ,  $1.25\pm 0.07$  and  $0.79\pm 0.04$ , respectively, i.e. aerosol

29 scattering coefficient and backscattering coefficient increased by 58 and 25% as the  
30 RH increased from 40 to 85%. Meanwhile, the aerosol hemispheric backscatter  
31 fraction decreased by 21%. The relative amount of organic matter (OM) or inorganics  
32 in  $PM_{10}$  was found to be a main factor determining the magnitude of  $f(RH)$ , the highest  
33 values of  $f(RH)$  corresponded to the aerosols with a small fraction of OM, and vice  
34 versa. The relative amount of  $NO_3^-$  in fine particles was strongly correlated to  $f(85\%)$ ,  
35 which suggests  $NO_3^-$  played a vital role in aerosol hygroscopic growth during this  
36 study. The mass fraction of nitrate also had a close relation to the curvature of  
37 humidograms, namely, the higher the nitrate concentration is, the straighter the  
38 humidogram will be. At 85% RH, the aerosol direct radiative forcing increased by 47%  
39 compared to that in dry conditions due to the aerosol hygroscopic growth.

## 40 **1 Introduction**

41 Hygroscopic aerosols take up water as humidity increases (Engelhart et al.,  
42 2011;Pilinis et al., 1989;Hänel, 1976;Covert et al., 1972). Aerosol water matters since  
43 water can affect both the size and refractive indices of atmospheric aerosols, thereby  
44 influencing the mass concentration, size distribution, and corresponding optical  
45 properties (e.g., scattering coefficient, backscattering coefficient, single scattering  
46 albedo, and asymmetry parameter) (Cheng et al., 2008;Randles et al., 2004;Malm et  
47 al., 2003;Carrico et al., 2003). In particular, understanding the effect of relative  
48 humidity on aerosol light scattering is important to better estimate the radiative  
49 forcing and evaluate visibility impairment (Ackerman et al., 2004;Tang,  
50 1996;Charlson et al., 1992;Covert et al., 1972). Besides, most of the ground-based  
51 aerosol measurements are conducted in dry conditions so as to have a consistency  
52 within networks. These measurements can differ significantly from the ambient ones.  
53 Thus, the determination of enhancement factors for various optical variables are of  
54 crucial importance for climate forcing calculations (Quinn et al., 1995;Pilinis et al.,  
55 1995) and the comparison between remote sensing and ground based measurements  
56 (Zhang et al., 2012;Wang and Martin, 2007;Zieger et al., 2012).

57 The Yangtze River Delta, one of the most populated and fastest growing regions

58 in China, has experienced extraordinary economic growth during the last two decades.  
 59 Amounting to 2.1% of the land area of China, this region contains ~11% of the  
 60 country's population and produces ~20% of China's Gross Domestic Product (GDP)  
 61 in 2013 (Wang et al., 2013). Concurrent with population increase and economic  
 62 growth are the increasing energy consumption and growing number of automobiles,  
 63 and therefore, the Yangtze River Delta has become a significant source of gas and  
 64 particulate pollutants and secondary aerosol production. A 5-week field campaign was  
 65 carried out in the early winter of 1999 at LinAn, a background station in the Yangtze  
 66 River Delta (Xu et al., 2002). However, since then the physical and chemical  
 67 properties of gas and particulate pollutants have changed dramatically with the rapidly  
 68 developing economy and fast growing population, e.g. from 1999 to 2013, the sulfate  
 69 mass concentration decreased from  $21.2 \pm 11.5$  to  $8.1 \pm 4.1$  (mean  $\pm$  SD) (Qi et al.,  
 70 2012; Xu et al., 2008; ZEPB, 1999; ZEPB, 2013). In order to better understand the  
 71 aerosol light scattering properties and their dependency on relative humidity in the  
 72 Yangtze River Delta, both the scattering and backscattering coefficients under dry  
 73 (RH<40%) conditions and controlled relative humidity were measured, along with the  
 74 chemical composition and particle number size distribution.

75 The enhancement factors discussed in this work include scattering enhancement  
 76 factor  $f(\text{RH}, \lambda)$ , enhancement factor for backscattering coefficient  $f_b(\text{RH}, \lambda)$  and  
 77 enhancement factor for hemispheric backscatter fraction  $f_\beta(\text{RH}, \lambda)$ . The impact of  
 78 relative humidity on the aerosol light scattering coefficient is defined as scattering  
 79 enhancement factor  $f(\text{RH}, \lambda)$ :

$$80 \quad f(\text{RH}, \lambda) = \sigma_{\text{sp}}(\text{RH}, \lambda) / \sigma_{\text{sp}}(\text{dry}, \lambda) \quad (1)$$

81 where  $\sigma_{\text{sp}}(\text{dry}, \lambda)$  and  $\sigma_{\text{sp}}(\text{RH}, \lambda)$  represent scattering coefficients at wavelength  $\lambda$  in dry  
 82 conditions and at a defined higher relative humidity, respectively.

83 Likewise, the impact of relative humidity on aerosol backscattering coefficient  
 84 can be described as enhancement factor for backscattering coefficient  $f_b(\text{RH}, \lambda)$ :

$$85 \quad f_b(\text{RH}, \lambda) = \sigma_{\text{bsp}}(\text{RH}, \lambda) / \sigma_{\text{bsp}}(\text{dry}, \lambda) \quad (2)$$

86 where  $\sigma_{\text{bsp}}(\text{dry}, \lambda)$  and  $\sigma_{\text{bsp}}(\text{RH}, \lambda)$  represent backscattering coefficients at wavelength  $\lambda$

87 in dry conditions and at a defined relative humidity, respectively.  $f(\text{RH},\lambda)$  and  $f_b(\text{RH},\lambda)$   
88 are always greater than 1 if no significant restructuring is taken place after water  
89 uptake (Weingartner et al., 1995).

90 Hemispheric backscatter fraction ( $b$ ) is closely related to the upscatter fraction  
91 ( $\bar{\beta}$ ), the fraction of incident solar radiation scattered into space (Wiscombe and Grams,  
92 1976). The impact of relative humidity on aerosol hemispheric backscatter fraction  
93 can be defined as enhancement factor for hemispheric backscatter fraction  $f_\beta(\text{RH},\lambda)$   
94 (Adam et al., 2012):

$$95 \quad f_\beta(\text{RH},\lambda) = b(\text{RH},\lambda)/b(\text{dry},\lambda) \quad (3)$$

96 where  $b(\text{dry},\lambda)$  and  $b(\text{RH},\lambda)$  represent hemispheric backscatter fraction at wavelength  
97  $\lambda$  in dry conditions and at the defined relative humidity.  $b$  is defined as the ratio of  
98 backscattering coefficient to scattering coefficient:  $b = \sigma_{\text{bsp}}/\sigma_{\text{sp}}$ . Thus,  $f_\beta(\text{RH},\lambda)$  can be  
99 rewritten as:  $f_\beta(\text{RH},\lambda) = f_b(\text{RH},\lambda)/f(\text{RH},\lambda)$ .

100 The wavelength dependence of scattering enhancement factor  $f(\text{RH},\lambda)$  varies  
101 with generalized aerosol types. Kotchenruther and Hobbs (1998) and Zieger et al.  
102 (2010; 2011) found no pronounced wavelength dependence of  $f(\text{RH},\lambda)$  for biomass  
103 burning aerosols and arctic aerosols, respectively; Zieger et al. (2013) found small  
104 variations (<5%) of  $f(\text{RH},\lambda)$  at 450, 550 and 700 nm for several European sites;  
105 Kotchenruther et al. (1999) and Magi and Hobbs (2003) reported significant  
106 wavelength dependence of  $f(\text{RH},\lambda)$  for urban/industrial aerosols off the east coast of  
107 the United States. In this study, the wavelength dependence of enhancement factors  
108 was also investigated. Except when specially mentioned, all the parameters discussed  
109 in this study are based on the measurements at 550 nm wavelength only.

110

## 111 **2 Experimental sites and instrumentation**

### 112 **2.1 Site description**

113 This study was carried out during an intensive field sampling period from 1 to 31  
114 March 2013 at LinAn Regional Atmosphere background station, which is a WMO  
115 GAW regional station (30.3° N, 119.73° E, 138 m a.s.l.) located in the center of

116 Yangtze River Delta, China (Fang et al., 2013) (as shown in Fig. 1). It is  
117 approximately 11 km north of the city of LinAn, with a population of 1.5 million. The  
118 site is ~50 km west of Hangzhou (capital of Zhejiang Province with a population of  
119 ~8.8 million) and ~210 km southwest of Shanghai (a mega-city with a population of  
120 ~20 million). LinAn station is on the top of a small hill, in an area primarily covered  
121 by bamboo forests and paddy rice fields, and represents the background conditions of  
122 the Yangtze River Delta. North of the station is a small village with ~200 inhabitants.  
123 In addition, there is an activated charcoal factory ~1.4 km north of LinAn station that  
124 uses bamboo wood as its source material (Qi et al., 2012). During the observation  
125 period, the prevailing winds were northeasterly (NE) and southwesterly (SW) with an  
126 average wind speed of  $\sim 2.5 \text{ m}\cdot\text{s}^{-1}$  (SD  $1.4 \text{ m}\cdot\text{s}^{-1}$ ). 72-hour back trajectories showed two  
127 contrasting air mass origins: (1) air masses from Northern China through  
128 long-distance transport and (2) air masses from southerly/southwesterly directions  
129 with a much shorter transport distance.

## 130 **2.2 Measurement system and data processing**

131 The scattering enhancement factor  $f(\text{RH})$  is defined as the ratio of aerosol  
132 scattering coefficient at a given, elevated RH to that at a low RH (usually  $<40\%$ ).  
133 Correspondingly, the humidification system included two nephelometers operating in  
134 series with a humidifier between them. Sample air entered the first nephelometer  
135 (reference nephelometer or DryNeph) through an aerosol dryer (Shen et al.,  
136 2011;Tuch et al., 2009) to ensure the aerosol was at dry conditions (RH inside  
137 DryNeph was  $12.2 \pm 3.4\%$  (mean  $\pm$  SD) for the whole field campaign), then passed  
138 through the humidifier, where the sample RH was regulated to a higher RH that was  
139 ramped from  $\sim 40$  to  $90\%$ , and finally entered the second nephelometer (humidified  
140 nephelometer or WetNeph) where the scattering coefficient of humidified aerosols  
141 was measured.

142 Aerosol total scattering (between  $7$  and  $170$  degrees) and backscattering  
143 coefficients (between  $90$  and  $170$  degrees) were measured by an integrating  
144 nephelometer (TSI Inc., Model 3563) at three wavelengths: blue ( $450 \text{ nm}$ ), green ( $550$   
145  $\text{nm}$ ) and red ( $700 \text{ nm}$ ). Data were recorded as 1-minute average and a zero check was

146 performed automatically once per hour. The detailed information of this instrument  
147 has been described in many previous studies (Anderson and Ogren, 1998; Charlson et  
148 al., 1969; Anderson et al., 1996).

149 The humidifier was built by the aerosol group in Global Monitoring Division,  
150 Earth System Research Laboratory, National Ocean & Atmospheric Administration,  
151 USA (NOAA/GMD), which was described in Carrico et al. (1998). It consists of 2  
152 concentric tubes with a heater and insulation around the outer tube. Sample air flows  
153 through the inner tube, while water circulates between the inner and outer tubes. The  
154 inner tube is made of porous extruded PTFE (polytetrafluoroethylene) membrane,  
155 whose pore size is large enough for water molecules, but too small for larger  
156 molecules such as oxygen to cross. The flux of water vapor through the membrane is  
157 controlled by regulating the electric current to the humidifier heater until the desired  
158 RH is attained. The humidity scan was a one-hour cycle; RH was ramped from ~40 to  
159 90% during the first half hour and in the reverse direction during the last half hour.

160 Besides the scattering measurement, particle number size distribution and aerosol  
161 chemistry were also measured at the station. Particle number size distributions from 3  
162 nm to 10  $\mu\text{m}$  were measured by a twin differential mobility particle sizer (TDMPS)  
163 (Birmili et al., 1999) and an aerodynamic particle sizer (APS, model 3321, TSI Inc.).  
164 The mass concentrations of sulfate, nitrate, ammonium, organic matter (OM) and  
165 chloride (aerodynamic diameter less than 1  $\mu\text{m}$ ) were measured by an aerosol mass  
166 spectrometer (AMS, Aerodyne Inc.). The equivalent mass concentration of black  
167 carbon (EBC) was measured by a multi angle absorption photometer (MAAP, mode  
168 5012, Thermo Scientific Inc.) at 637 nm wavelength (Müller et al., 2011), the  
169 assumed mass absorption cross-section was  $6.6 \text{ m}^2 \cdot \text{g}^{-1}$ . Visibility was measured using  
170 a near-forward scattering sensor (FD12, Vaisala). Meteorological data were provided  
171 by the LinAn Regional Atmosphere Background Station.

172 All the instruments were housed in a measurement laboratory where room  
173 temperature was controlled at  $\sim 25 \text{ }^\circ\text{C}$ . All data were reported in Beijing Time  
174 (BJT=UTC+8 h) and all the scattering data were referenced at  $T=0 \text{ }^\circ\text{C}$  and  $P=1013.25$   
175 hPa. Truncation error correction, proposed by Anderson and Ogren in 1998 (Anderson

176 and Ogren, 1998), was applied to retrieve the final scattering and backscattering  
177 coefficients. The Ångström exponent  $\alpha$  was defined as  
178  $\alpha = -\log[\sigma_{sp}(\lambda_1)/\sigma_{sp}(\lambda_2)]/\log[\lambda_1/\lambda_2]$ . It represented the wavelength dependence of light  
179 scattering assuming a power law relationship of  $\sigma_{sp}$  and  $\sigma_{bsp}$ . In this study, scattering  
180 coefficients at 450 nm and 700 nm were used to derive  $\alpha$ . Normalization of f(RH)  
181 (Day and Malm, 2001) has been carried out to get the final f(RH) scan values, i.e.  
182 f(40%) (the lowest RH in one cycle) is set to 1 and used to normalize other f(RH)  
183 values in this cycle. It's worth mentioning that the normalization of f(RH) (see Sect.  
184 2.2) may underestimate f(RH) to some extent, since some organics (e.g. humic acid  
185 sodium) take up water even when RH <40% (Sjogren et al., 2007; Dick et al., 2000).  
186 To evaluate its impact, we calculated the raw f(40%) value without the normalization.  
187 The average and standard deviation were 1.03 and 0.03 with a maximum of 1.08,  
188 which means this normalization may cause an underestimate of 5% (an error of 3%  
189 was caused by the inconsistency of DryNeph and WetNeph, see Sect. 2.4) at most.  
190 Figure 2c shows the un-normalized f(RH) value, the lowest value of each cycle was  
191 around 1.03, considering the inconsistency of DryNeph and WetNeph, f(RH) is close  
192 to unity at the lowest RH (~40%).

### 193 **2.3 Inlet system**

194 An automatic regenerating adsorption aerosol dryer (Tuch et al., 2009) was used  
195 to provide low RH sample air to DryNeph, TDMPs, APS, AMS and MAAP to ensure  
196 comparability of measurements. The aerosol dryer was housed in a separate shelter  
197 which was located on the rooftop (~ 5 m a.g.l.) of the measurement laboratory.  
198 Aerosols entered the shelter through a commercially available PM<sub>10</sub> impactor (PM<sub>10</sub>  
199 inlet, URG Corporation). Then these particles went through the adsorption aerosol  
200 dryer (Tuch et al., 2009) to ensure the RH less than 30%. The dried aerosols passed  
201 through a splitter via 3/4" stainless steel tubes, and then reached different instruments.  
202 The total sample flow through this dryer inlet was kept at 16.7 lpm to ensure a 50%  
203 collection efficiency at 10  $\mu$ m aerodynamic diameter (Berner et al., 1979). Since a lot  
204 of instruments share the total flow, the sample flow for the nephelometer is 9 lpm.

### 205 **2.4 Quality control on scattering measurements**

206 Accurate performance of nephelometers and RH sensors is crucial to retrieve  
207 reliable enhancement factors ( $f(\text{RH},\lambda)$ ,  $f_b(\text{RH},\lambda)$  and  $f_\beta(\text{RH},\lambda)$ ), since they are defined  
208 as the ratio of aerosol scattering coefficient/ backscattering coefficient/ hemispheric  
209 backscatter fraction at a higher RH to those at a low RH (usually <40%). In addition,  
210 the RH control in the WetNeph sensing volume is also critical to  $f(\text{RH})$  measurement.  
211 Therefore, several comparisons and calibrations have been carried out before and  
212 during the experiment. Three external RH sensors (Vaisala, model HMP60) were  
213 calibrated in the RH range of 11% to 80% using Vaisala Humidity Calibrator  
214 (HMK15) with four saturated salt solutions (LiCl,  $\text{K}_2\text{CO}_3$ , NaCl,  $(\text{NH}_4)_2\text{SO}_4$ ), and  
215 humidity/temperature transmitter (Vaisala, model HMT333), which was calibrated by  
216 the National Center for Meteorological Metrology, China. Two internal nephelometer  
217 RH sensors were calibrated to the external RH sensors with an uncertainty of  $\leq 2\%$ . A  
218 good agreement of these RH sensors was achieved with the discrepancy <3%. Both  
219 nephelometers were calibrated with  $\text{CO}_2$  (purity 99.999%) and filtered air. Filtered air  
220 measurements were made automatically every hour to track the instrument stability.  
221 Comparison of scattering and backscattering coefficients of the two nephelometers  
222 under low RH ( $9.6 \pm 3.2\%$ ) was performed during 1 to 3 March, 2013 (as shown in Fig.  
223 2). The total scattering coefficient and backscattering coefficient measured by  
224 WetNeph were constantly 3% ( $y=1.03x+1.60$ ,  $R^2=1.000$ ) and 4% ( $y=1.04x+0.09$ ,  
225  $R^2=0.997$ ) higher than those obtained by DryNeph at 550 nm (similarly for other  
226 wavelengths), the high consistency demonstrates that the two nephelometers were  
227 operating quite steadily and the scattering/backscattering coefficients measured by  
228 DryNeph can be corrected in order to make them comparable to the measurements of  
229 WetNeph. The uncertainty of nephelometer measurements was  $\sim 10\%$  (Anderson et al,  
230 1996), combining the uncertainty of the measurements of the internal RH sensor, the  
231 uncertainty of  $f(85\%)$  was  $\sim 20\%$  at large, which may decrease for less hygroscopic  
232 particles or smaller RHs.

233 The RH at the outlet of WetNeph was regulated via a feedback system between  
234 the Vaisala RH signal, a PID controller and a heater. The humidifier set point was  
235 stepped from low to high RH and back to low RH every hour with the set point



236 changing every one or two minutes. Figure 2 is an example of our data showing the  
237 relative humidity control and corresponding scattering measurements. As can be seen  
238 from Fig. 2, good relative humidity control was achieved no matter whether the  
239 scattering/backscattering coefficient was high or low.

240 The nephelometers were operated at a constant flow of 20 lpm, comprised of 9  
241 lpm sample air and 11 lpm particle-free air (dilution flow). The total flowrate through  
242 the nephelometer was controlled by a mass flow controller. The dilution flow was  
243 regulated by a needle valve and measured by a mass flowmeter. The sample and  
244 dilution flow have been calibrated with a Gilibrator bubble flowmeter before the  
245 experiment. Filtered air tests have also been conducted to make sure that all the  
246 instruments were in good condition and that there were no leaks in the system.

247

## 248 **3 Results and discussion**

### 249 **3.1 Overview**

250 Figure 3 shows the time series of the measured and derived aerosol variables in  
251 March 2013, as well as the ambient RH and visibility. The scattering enhancement  
252 factor  $f(85\%)$  ranged from 1.29 to 1.86 (as shown in Fig. 3a) with an average of 1.58  
253 (Table 1) for the whole campaign. During 4-9 March,  $f(85\%)$  stayed at a low value of  
254  $1.42 (\pm 0.05)$  when LinAn was dominated by air masses from the south under clear sky.  
255 In March, the hourly averaged aerosol scattering coefficient under dry conditions  
256 (shown in Fig. 3c) varied from 21 to  $1067 \text{ Mm}^{-1}$  and the maximum occurred on 16  
257 March, when a severe haze occurred. The mean value and standard deviation of the  
258 hourly averaged aerosol scattering coefficient was  $223 \text{ Mm}^{-1}$  ( $140 \text{ Mm}^{-1}$ ). Visibility  
259 (Fig. 3b) varied from 0.1 km to 23.7 km with a mean value of 6.2 km. It was quite low  
260 on 23 and 24 March because the station was in cloud. From 15 to 16 March, visibility  
261 declined to 4.4 km with the accumulation of pollutants in the atmosphere, which was  
262 a severe haze episode (as mentioned above). An air mass from Northwest China with  
263 high dust levels arrived at LinAn on 10 March, with an abrupt increase of the aerosol  
264 scattering coefficient (Fig. 3c) and a sharp decline of Ångström exponent (Fig. 3d).

265 Based on nephelometer measurements, the enhancement factors for scattering

266 coefficient  $f(\text{RH})$ , backscattering coefficient  $f_b(\text{RH})$  and hemispheric backscatter  
267 fraction  $f_\beta(\text{RH})$  were determined by Eq. (1), (2) and (3), respectively. As can be seen  
268 from Table 1, their values at different RHs (50, 60, 70, 80 and 85%) were obtained  
269 using linear interpolation from the half-hourly humidogram data. The enhancement  
270 factors  $f(\text{RH})$  and  $f_b(\text{RH})$  increased as the RH increased, but  $f_b(\text{RH})$  increased much  
271 more slowly than  $f(\text{RH})$ . The  $f(85\%)$  and  $f_b(85\%)$  were 1.58 and 1.25, respectively,  
272 suggesting that the scattering coefficient and backscattering coefficient at 85% RH  
273 were 58 and 25% higher than those in dry conditions due to aerosol water uptake. The  
274  $f_\beta(\text{RH})$  decreased with increasing RH, i.e. hemispheric backscatter fraction becomes  
275 smaller with the increase of RH and the fraction of radiation that would be  
276 backscattered into space was reduced. The  $f_\beta(\text{RH})$  decreased  $\sim 21\%$  as the RH  
277 increased from 40 to 85%. All these parameters are of crucial importance in  
278 evaluating the aerosol radiative forcing.

279 Generally, the scattering enhancement factor ( $f(80\%)=1.44$ ) is much lower than  
280 the result ( $f(80\%)=1.7-2.1$ ) obtained by Xu et al. (2002) for LinAn in 1999. This value  
281 is also lower than the results obtained by Carrico during ACE-1 (Carrico et al., 1998)  
282 and ACE-Asia (Carrico et al., 2003), the values obtained by Zieger et al. (2013) in  
283 several European sites and the Arctic, as well as the values achieved by Malm and  
284 Day (Malm et al., 2005;Malm et al., 2003;Malm and Day, 2001;Day and Malm,  
285 2001;Malm and Day, 2000) in America. However, the difference between measured  
286  $f(\text{RH})$  in this study and previous studies performed in China (Yan et al., 2009;Pan et  
287 al., 2009;Liu et al., 2009;Delene and Ogren, 2002;Cheng et al., 2008) are much  
288 smaller. The enhancement factor for backscattering coefficient and hemispheric  
289 backscatter fraction ( $f_b(85\%)$  and  $f_\beta(85\%)$ ) is 1.25(0.07) and 0.79(0.04), respectively,  
290 similar to the results ( $f_b(82\%)=1.22\pm 0.06$  and  $f_\beta(82\%)=0.83$ ) obtained by Carrico at  
291 Sagres, Portugal during ACE-2 (Carrico et al., 2000) and the results ( $f_b(82\%)=1.27$   
292 and  $f_\beta(82\%)=0.75$ ) obtained by Carrico et al. (2003) during the dust-dominant period  
293 in ACE-Asia.

### 294 **3.2 Aerosol chemical properties**

295 The submicron mass concentration of sulfate, nitrate, ammonium, chloride and

296 organic matter (OM) measured by AMS and EBC in PM<sub>10</sub> measured by MAAP are  
297 summarized in Table 2. The mass concentration of OM is the largest, while the mass  
298 concentration of chloride is the smallest, in accord with previous studies in LinAn  
299 (Meng et al., 2012; Yan et al., 2005). The mean mass concentration of nitrate and  
300 sulfate were  $9.8 \pm 12.1 \mu\text{g}\cdot\text{m}^{-3}$  and  $8.1 \pm 4.1 \mu\text{g}\cdot\text{m}^{-3}$  in this study, similar to the values  
301 ( $9.4 \pm 7.1 \mu\text{g}\cdot\text{m}^{-3}$  for nitrate and  $8.6 \pm 3.7 \mu\text{g}\cdot\text{m}^{-3}$  for sulfate in PM<sub>2.5</sub>) at LinAn in 2010  
302 summer (Meng et al., 2012).

303 Aerosol acidity is a key parameter affecting aerosol hygroscopic growth. It is  
304 usually examined by comparing the  $\text{NH}_4^+$  mass concentration measured by AMS and  
305 the amount needed to fully neutralize sulfate, nitrate and chloride ions ( $\text{NH}_4^+$ <sub>predicted</sub>)  
306 (Sun et al., 2010):

$$307 \quad \text{NH}_4^+_{\text{predicted}} = 18 \times (2 * \text{SO}_4^{2-}/96 + \text{NO}_3^-/62 + \text{Cl}^-/35.5) \quad (4)$$

308 Figure 4 illustrates the relationship of measured  $\text{NH}_4^+$  and predicted  $\text{NH}_4^+$ . As  
309 shown in Fig. 4, the regression slope is close to 1, which implies that there was  
310 sufficient  $\text{NH}_3$  in the atmosphere to neutralize  $\text{H}_2\text{SO}_4$ ,  $\text{HNO}_3$  and  $\text{HCl}$ , and that the  
311 PM<sub>1</sub> aerosol at LinAn was bulk neutralized during the measurement period. Therefore,  
312 the dominant chemical form of sulfate aerosol is ammonium sulfate (AS) rather than  
313 acidic sulfate ( $\text{H}_2\text{SO}_4$  or  $\text{NH}_4\text{HSO}_4$ ) and the nitrate existed in the form of  $\text{NH}_4\text{NO}_3$   
314 (AN). By calculating Pearson's correlation coefficient among 5 different chemical  
315 compositions, it could be found that  $\text{NH}_4^+$  and  $\text{NO}_3^-$  are strongly correlated with  
316  $r=0.93$ ;  $\text{NH}_4^+$  and  $\text{SO}_4^{2-}$ ,  $\text{Cl}^-$  are highly related with  $r$  equal to 0.77 and 0.74  
317 respectively, which also implies the main form of inorganics would be  $\text{NH}_4\text{NO}_3$ ,  
318  $(\text{NH}_4)_2\text{SO}_4$  and  $\text{NH}_4\text{Cl}$ . However, because the average mass concentration of chloride  
319 was very low (see Table 2) at LinAn, it suggests that  $\text{NH}_4\text{NO}_3$  and  $(\text{NH}_4)_2\text{SO}_4$  are the  
320 dominant water-soluble ionic species, which are consistent with previous results at  
321 LinAn based on filter chemical measurements (Meng et al., 2012).

### 322 **3.3 Wavelength dependence of the scattering enhancement factor f(85%)**

323 The wavelength dependence of scattering enhancement factor is needed to  
324 estimate the aerosol radiative forcing since solar radiation at Earth's surface depends

325 on wavelength. The histogram for  $f(85\%, 550 \text{ nm})$  is shown in Fig. 5. Overlaid on the  
326 histogram for  $f(85\%, 550 \text{ nm})$  (Fig. 5) are Gaussian curves based on the statistics for  
327  $f(85\%)$  at each wavelength. No apparent shift of mean  $f(85\%)$  is seen for the 550 nm  
328 and 700 nm wavelength pair (see Fig. 5); while the mean  $f(85\%, 450 \text{ nm})$  is ~6%  
329 lower than that at 550 nm with a smaller standard deviation (see Fig. 5). For higher  
330 values (90th and 70th percentile values in Table 3), slightly wavelength dependence of  
331  $f(\text{RH})$  can be observed, i.e. the  $f(\text{RH})$  increases with the increase of wavelength.  
332 However, the differences are mostly under 10% and therefore the discussion is  
333 focused on 550 nm wavelength in this study. Similar results were obtained by Zieger  
334 at a regional continental research site at Melpitz, Germany (Zieger et al., 2014).

### 335 **3.4 Classification of various observation episodes**

336 Based on wind direction, back trajectory analysis and weather phenomenon,  
337 observation periods can be classified into three main sectors: a northerly-polluted  
338 period (influenced by long-distance transport from northern China), a locally-polluted  
339 period, and a dust-influenced episode. Air mass back trajectories over 72 hours at  
340 300m a.g.l. arrival height were calculated using the Trajectory Statistics (TrajStat)  
341 model (Wang et al., 2009) with 6-hourly archived meteorological data provided by the  
342 US National Centers for Environmental Prediction (NCEP). The characteristics of  
343 these three periods are as follows:

- 344 1. Periods when the wind direction is between  $120^\circ$  and  $270^\circ$  are chosen as  
345 “locally-polluted periods”. During this period, pollutants mostly came from Anhui  
346 province, Jiangxi province and the southern region of Zhejiang province as well as  
347 LinAn (green line in Fig. 6). Economy in these areas is mainly made up of  
348 manufacturing, tourism and agriculture.
- 349 2. Periods when the wind direction is greater than  $270^\circ$  or less than  $120^\circ$  are  
350 described as “northerly-polluted periods”. Back trajectories indicate that most of  
351 the air masses came from northern China and passed over heavily polluted areas  
352 such as the Beijing-Tianjin-Tangshan economic region and the Yangtze River  
353 Delta during long-distance transport (red line in Fig. 6).
- 354 3. A heavy dust event occurred at LinAn on 10 March (approximately from 02:00

355 BJT) according to satellite information (<https://earthdata.nasa.gov/labs/worldview/>)  
356 and meteorology information (provided by China Meteorological Administration,  
357 CMA). The 72 h back trajectory shows the air masses tracked from Mongolia and  
358 passed over Inner Mongolia (blue line in Fig. 6).

### 359 **3.4.1 Locally-polluted period**

360 In the periods of 4-9, 15-20 and 26-30 March, 2013 aerosols were mainly from  
361 locally mixed pollutants from Zhejiang and/or nearby provinces. The mean  $f(80\%)$   
362 and  $f(85\%)$  were 1.36 and 1.52 (as shown in Table 4), ~10 and 8% lower than those in  
363 northerly-polluted periods.

364 The enhancement factor for scattering coefficient and backscattering coefficients  
365 at 80% during locally-polluted period is 1.36 and 1.15, respectively, similar to the  
366 values ( $f(82.5\%)=1.4-1.5$ ) and ( $f_{\beta}(82.5\%)=1.1-1.2$ ) obtained by Koloutsou-Vakakis et  
367 al. (2001) at a northern hemisphere, continental site (Bondville, Illinois, US). The  
368 measured dry scattering coefficient is  $217 \text{ Mm}^{-1}$ , ~15% lower than that of the  
369 northerly-polluted period ( $251 \text{ Mm}^{-1}$ ). The averaged mass percentage of sulfate,  
370 nitrate, ammonium, OM, chloride and EBC are 17.6, 16.1, 13.0, 42.2, 1.5 and 9.6%,  
371 respectively (shown in Fig. 6a). Compared to the northerly-polluted period, the mass  
372 percentage of OM is ~27% higher during the locally-polluted period, while the mass  
373 percentage of nitrate is ~33% lower. Although the  $\text{OM}/(\text{OM}+\text{SO}_4^{2-})$  ratios during  
374 locally-polluted period (~0.70) and northerly-polluted period (~0.67) are similar, the  
375  $\text{OM}/(\text{OM}+\text{NO}_3^-+\text{SO}_4^{2-})$  ratio during locally-polluted period (~0.56) is 24% higher  
376 than that during northerly-polluted period (~0.45), which may partly explain the lower  
377  $f(\text{RH})$  during locally-polluted episode (as discussed later in Sect. 3.5).

### 378 **3.4.2 Northerly-polluted period**

379 The air masses reaching LinAn during the period March 1-3, 11-15, 20-26 and  
380 30-31 (dust episode excluded) mainly came from northern China through  
381 long-distance transport. The mean  $f(80\%)$  and  $f(85\%)$  were 1.50 and 1.64,  
382 respectively (as shown in Table 4).

383 The value ( $f(80\%)=1.50$ ) is similar to the previous results ( $f(80\%)=1.48$ )  
384 obtained by Yan et al. (2009) for periods under the downwind of urban plume from

385 Beijing, ( $f(80\%)=1.46\pm 0.10$ ) reported by Carrico et al. (2000) for anthropogenic  
386 aerosols in Europe during the 2<sup>nd</sup> Aerosol Characterization Experiment (ACE-2)  
387 campaign, and ( $f(80\%)=1.55-1.59$ ) indicated by Pan et al. (2009) for a rural site  
388 (Xin'an) near Beijing city during pollution periods. However, the measured  $f(80\%)$   
389 was much lower than ( $f(80\%)=2.0-2.43$ ) during a pollution episode reported by Kim  
390 et al. (2006) at the Gosan regional background site, 720 km northeast of LinAn and  
391 results ( $f(82\%)=2.24\pm 0.20$ ) obtained by Carrico et al. (2003) in ACE-Asia for polluted  
392 air masses measured over the ocean. The  $f(RH)$  of continental air masses transported  
393 over the ocean was higher than that over the continent, and the possible mechanisms  
394 for that increase might include coagulation with sea-salt particles and the oxidation of  
395  $SO_2$  and VOCs (volatile organic compounds) leading to an increase in the particle's  
396 hygroscopicity.

### 397 **3.4.3 Dust-influenced episode**

398 During a severe cold air outbreak, a strong dust event struck northern China on 8  
399 and 9 March, 2013. The affected area covered about 2.8 million square kilometers,  
400 about 0.27 million square kilometers of which suffered from dust storms or strong  
401 sandstorms. This event was considered to be the largest and strongest dust event to hit  
402 China in 2013. During this process, suspended dust appeared in most of northwestern  
403 China, northern China, north and west Huanghuai region and west Liaoning province,  
404 the west-central Inner Mongolia, west Gansu, northern Shanxi, and several parts of  
405 Xinjiang experienced a sandstorm. Along with the extreme dust event, there was a  
406 dramatic increase in  $PM_{10}$ , for example, the  $PM_{10}$  in Yulin, Shanxi even reached  
407  $10,000 \mu\text{g}\cdot\text{m}^{-3}$  (Wang et al., 2013; Zhang and Sun, 2013).

408 At 2 a.m. on March 10, wind direction changed abruptly to northerly (see Fig.  
409 8d). The scattering coefficient increased abruptly from  $\sim 200 \text{Mm}^{-1}$  to  $> 600 \text{Mm}^{-1}$  (see  
410 Fig. 7b).  $PM_{10}$  mass concentrations at LinAn increased rapidly from  $100 \mu\text{g}\cdot\text{m}^{-3}$  to  $637$   
411  $\mu\text{g}\cdot\text{m}^{-3}$ , while the  $PM_{2.5}$  mass concentration was only  $190 \mu\text{g}\cdot\text{m}^{-3}$ , accounting for 30%  
412 of  $PM_{10}$ . The Ångström exponent decreased from 1.2 to 0.8 (see Fig. 7c). All these  
413 phenomena implied the arrival of cold front from northern China enriched in coarse  
414 mode particles. The mass percentage of nitrate increased significantly and reached its

415 peak (~26%) at 3 a.m.; meanwhile, the mass percentage of OM decreased sharply  
416 from 2 a.m. to 3 a.m. (see Fig. 7e). Correspondingly, the scattering enhancement  
417 factor  $f(85\%)$  reached 1.52 at 3 a.m. (see Fig. 7a), an increase of ~16% compared with  
418 that before the dust arrival. The most dust-dominated period, from 7 a.m. to 1 p.m.,  
419 when the Ångström exponent was below 0.5 (Fig. 7c) and scattering coefficients at  
420 450 nm, 550 nm and 700 nm (Fig. 7b) were almost the same, the scattering  
421 enhancement factor  $f(85\%)$  was ~1.46. This value is much higher than the results  
422 ( $f(80\%)=1.20$ ) reported by Pan et al. (2009) in rural Beijing, ( $f(82.5\%)=1.18$ )  
423 obtained by Carrico et al. (2003) in East Asia (ACE-Asia) during a dust episode,  
424 ( $f(80\%)=1.20$ ) reported by Fierz-Schmidhauser et al. (2010) at a high alpine site  
425 (Jungfrauoch, 3580m a.s.l.) in Switzerland during a strong Saharan dust event, and  
426 ( $f(80\%)=1.0-1.1$ ) measured by Li-Jones et al. (1998) in South America during an  
427 investigation of long-range transported Saharan dust. Meanwhile it is much lower  
428 than the value ( $f(85\%)=1.73-2.20$ ) obtained by Kim et al. (2006) in Gosan (South  
429 Korea) during a dust-dominated period. According to Tobo et al. (2010), Ca-rich  
430 particles can react with gaseous  $\text{HNO}_3$  to form  $\text{Ca}(\text{NO}_3)_2$ , thus the liquid  
431 cloud-nucleating ability would be enhanced. Similar results have also reported that  
432 aerosol hygroscopicity would be largely enhanced if coarse mode Ca-rich particles  
433 combined with nitrate (Shi et al., 2008; Sullivan et al., 2009). Thus, it is speculated  
434 that the relatively high  $f(\text{RH})$  may have resulted from the reactions of coarse mode  
435 particles with inorganics (very likely to be nitrate) during long-range transport.

### 436 **3.5 The relationship of scattering enhancement factor with chemical** 437 **compositions**

438 Scattering enhancement factor  $f(85\%)$  versus organic mass fraction and inorganic  
439 mass fraction were shown in Fig. 8. The total mass concentration was calculated as  
440 the sum of mass concentrations of sulfate, nitrate, ammonium, chloride and organic  
441 measured by AMS and EBC measured by MAAP. The organic and inorganic mass  
442 fractions were calculated by dividing the mass concentration of organics (measured  
443 by AMS) and inorganics (the sum of sulfate, nitrate, ammonium and chloride  
444 measured by AMS) by the total mass concentration, respectively. The bivariate linear

445 regression was applied with the uncertainty of  $f(85\%, 550\text{nm})$  which was discussed in  
446 Sect. 2.4 and the standard deviation of chemical compositions. The bivariate linear  
447 regressions (Fig. 8) show clearly anti-correlation of  $f(85\%, 550\text{nm})$  to organics  
448 fraction and strongly positive correlation of  $f(85\%, 550\text{nm})$  to inorganics fraction.  
449 This implies that chemical composition plays a vital role in aerosol hygroscopic  
450 properties. The absolute values of both slopes (1.2 for  $f(85\%)$  vs. organic mass  
451 fraction and 0.96 for  $f(85\%)$  vs. inorganic mass fraction) were much lower than those  
452 (3.1 and 2.2, respectively) measured at Melpitz, Germany (Zieger et al., 2014). This  
453 may partly account to the higher organic (or lower inorganic) contents at LinAn.  
454 Comparing Fig. 8 (a)(b) and (c)(d), a more clearly trend of increasing nitrate with  
455 increasing  $f(85\%)$  was observed. The role nitrate plays in aerosol hygroscopic  
456 properties will be discussed in the following paragraph.

457  $f(\text{RH})$  in Fig. 9 was expressed in terms of  $\gamma$  so as to be applied to a broader RH  
458 range (Doherty et al., 2005; Quinn et al., 2005):  $\gamma = \ln f(\text{RH}) / \ln((100 - \text{RH}_{\text{ref}}) / (100 - \text{RH}))$ .  
459 Here  $\gamma$  was based on  $\text{RH}_{\text{ref}} = 40\%$  and  $\text{RH} = 85\%$ . The relative amount of OM and  
460 inorganics can be expressed as  $F_o = C_c / (C_c + C_i)$ , where  $C_c$  and  $C_i$  are the mass  
461 concentrations of OM and inorganics, respectively. Figure 9 shows  $\gamma$  versus  $F_o$  where  
462  $C_i$  was the mass concentrations of  $\text{SO}_4^{2-}$ ,  $\text{NO}_3^-$  and  $\text{NO}_3^- + \text{SO}_4^{2-}$  in Fig. 9a, Fig. 9b  
463 and Fig. 9c, respectively. For all the three scatter plots, there is a trend of decreasing  $\gamma$   
464 with increasing  $F_o$ . However, unlike the results of Quinn et al. (2005), Malm et al.  
465 (2005), Pan et al. (2009) and Yan et al. (2009),  $\gamma$  and  $F_o$  ( $\text{OM} / (\text{OM} + \text{SO}_4^{2-})$ ) (shown in  
466 Fig. 9a) were uncorrelated ( $R^2 = 0.14$ ), while  $\gamma$  and  $F_o$  ( $\text{OM} / (\text{OM} + \text{NO}_3^-)$ ) (shown in Fig.  
467 9b) and  $\gamma$  and  $F_o$  ( $\text{OM} / (\text{OM} + \text{SO}_4^{2-} + \text{NO}_3^-)$ ) (shown in Fig. 9c) were more strongly  
468 correlated ( $R^2$  of 0.56 and 0.68, respectively). This result implies that  $\text{NO}_3^-$  (rather  
469 than  $\text{SO}_4^{2-}$ ) plays an important role in aerosol hygroscopic growth during this study..  
470 This increasingly importance of nitrate corresponds to many recent studies in  
471 Shanghai (a mega city in Yangtze River Delta) (Shi et al., 2014) and Beijing (Sun et  
472 al., 2012). This may partly result from increasing availability of  $\text{NH}_3$  to form  $\text{NH}_4\text{NO}_3$   
473 (Morgan et al., 2010) due to the decrease of  $\text{SO}_2$ . Chinese government has put an  
474 emphasis on the control of  $\text{SO}_2$  emission in recent years. The desulfurization



475 technology were installed at coal-fired power units as well as certain steel and cement  
476 production facilities, as a result, the annual average concentration of SO<sub>2</sub> decreased  
477 significantly from 56 to 19 μg·m<sup>-3</sup> at LinAn from 2006 to 2012 (ZEPB, 2012; 2006).

478 The molar ratio of particulate SO<sub>4</sub><sup>2-</sup> to total sulfur (SO<sub>4</sub><sup>2-</sup>+gas phase SO<sub>2</sub>) was  
479 used as an indicator of the relative age of aerosols (Quinn et al., 2005). For relatively  
480 younger aerosols, there is insufficient time for the conversion of SO<sub>2</sub> to SO<sub>4</sub><sup>2-</sup> via gas  
481 and aqueous phase oxidation process and therefore the SO<sub>4</sub><sup>2-</sup>/(SO<sub>4</sub><sup>2-</sup>+SO<sub>2</sub>) molar ratio  
482 is low. As aerosol ages, more SO<sub>2</sub> is converted to SO<sub>4</sub><sup>2-</sup> and thus the ratio increases.  
483 To illustrate the effects of this ratio and scattering coefficient on γ, Fig. 10 shows γ  
484 versus Fo=OM/(OM+SO<sub>4</sub><sup>2-</sup>+NO<sub>3</sub><sup>-</sup>) colored by the SO<sub>4</sub><sup>2-</sup>/(SO<sub>4</sub><sup>2-</sup>+SO<sub>2</sub>) molar ratio (Fig.  
485 10a) and log<sub>10</sub>(σ<sub>sp</sub>) (Fig. 10b). The highest values of γ ( or f(RH)) corresponded to  
486 more aged aerosols with a low OM content ; while the lowest values corresponded to  
487 younger aerosols with a higher OM content, consistent with the result of Quinn et al.  
488 (2005). For aerosols with relatively low scattering coefficient, the value of f(RH) was  
489 usually low with a large variation (dots with cooler colors in Fig. 10b); while aerosols  
490 with high scattering coefficients, the value of f(RH) was relatively high with a small  
491 variation(dots with warm colors in Fig. 10b).

### 492 **3.6 Parameterization of scattering enhancement factor f(RH)**

493 Scattering enhancement factor f(RH) can be parameterized using empirical  
494 equations (Kotchenruther and Hobbs, 1998; Kotchenruther et al., 1999; Gassó et al.,  
495 2000; Carrico et al., 2003; Liu et al., 2008; Pan et al., 2009; Zieger et al., 2010; Zieger  
496 et al., 2014). Humidograms of LinAn were fitted into two empirical equations and the  
497 fitting results were shown below.

#### 498 **3.6.1 Parameterization with equation f(RH)=c (1-RH)<sup>-g</sup>**

499 Kasten (1969) proposed an empirical equation f(RH)=c (1-RH)<sup>-g</sup> to describe how  
500 f(RH) varies with RH, which has been used in previous reports e.g. by Kotchenruther  
501 and Hobbs (1998), Gassó et al. (2000), Carrico et al. (2003) and Zieger et al. (2010,  
502 2014). Table 5 shows the fitting results of this work and other previous studies. The  
503 larger “c” and “g”, the larger f(RH). In this work, “g” was much lower than that in  
504 most of the other studies, while was similar to the result of Gassó et al. (2000) during

505 dust episode. It results from the comparably low scattering enhancement factor (e.g.  
506  $f(80\%)=1.44\pm 0.12$ ) of LinAn, which was similar to the value ( $f(80\%)=1.33\pm 0.07$ )  
507 obtained by Gassó et al. (2000) for a dust event. The  $f(\text{RH})$  in other studies was much  
508 higher than that at LinAn, ranging from 2.04 (polluted marine aerosols in Gassó et al.  
509 (2000)) to 3.77 (arctic aerosols in Zieger et al. (2010)), therefore their parameter “g”  
510 was much higher.

### 511 **3.6.2 Parameterization with equation $f(\text{RH})=1+a \text{RH}^b$**

512 The  $f(\text{RH})$  obtained at LinAn station can be well described by the following  
513 equation, which was proposed by Kotchenruther and Hobbs (1998):

$$514 \quad f(\text{RH})=1+a \text{RH}^b \quad (5)$$

515 where “a” is positive and “b” is greater than 1. This function is convex, and has been  
516 used in many previous studies (Pan et al., 2009;Delene and Ogren, 2002;Carrico et al.,  
517 2003;Kotchenruther et al., 1999;Kotchenruther and Hobbs, 1998) to describe  
518 monotonic growth. Theoretically, parameter “a” determines the largest value  $f(100\%)$   
519 can reach, and parameter “b” dominates the curvature of the function. The smaller “b”  
520 is, the smaller the curvature of humidogram will be; if “b” equals to 1, then  
521  $f(\text{RH})=1+a \text{RH}$ . The parameters “a” and “b” from our study and previous results for  
522 different aerosol types are listed in Table 6. Taking the locally-polluted episode as an  
523 example, although parameter “a” is slightly larger (~3%) than in northerly-polluted  
524 episode, parameter “b” is ~40% larger, as a result the  $f(85\%)$  during locally-polluted  
525 period is smaller. Parameter “b” is the largest in the locally-polluted episode, and  
526 smallest in the northerly-polluted period, i.e. the curvature of  $\text{RH}-f(\text{RH})$  line is largest  
527 during the locally-polluted episode, then is the dust episode, and northerly-polluted  
528 period is the smallest, which is consistent with the mass percentages of nitrate (see  
529 Fig. 6) (will be discussed later).

### 530 **3.6.3 Steepness of humidograms**

531 Among all the humidograms measured at LinAn,  $f(\text{RH})$  increases continuously  
532 and monotonically. However, the curvatures of different humidograms are different  
533 (Fig. 11): some increase with a nearly constant rate and the humidogram line is almost  
534 straight, while some increase slowly at first and then increase more steeply at

535 relatively higher RH, thus the curvature of the humidogram is larger. In order to  
 536 describe the growth pattern quantitatively, a steepness index  $\eta$  is defined based on the  
 537 fitting curve:

$$538 \quad \eta = f'(80\%) / f'(60\%) - 1 = (4/3)^{b-1} - 1 \quad (6)$$

539 where  $f'(60\%)$  and  $f'(80\%)$  represent the derivatives of the fitting curve at 60% and 80%  
 540 RH, respectively.  $\eta$  is a nonnegative number. Zieger et al. (2010) has defined an index  
 541 describing the magnitude of deliquescence transitions based on fitting equation  
 542  $f(\text{RH}) = (1 - \text{RH})^{-g}$  (see Sect. 3.6.1), while the steepness index  $\eta$  proposed in this study  
 543 provided a way of quantitatively describing the steepness of humidograms well fitted  
 544 into equation  $f(\text{RH}) = 1 + a \text{RH}^b$ . The larger  $\eta$  is, the bigger the curvature. As is shown in  
 545 Fig. 11a, for a large  $\eta$ , the  $f'(60\%)$  is very small, meaning that aerosol scattering  
 546 coefficient barely increases ( $f(\text{RH}) \approx 1$ ) under low RH (usually  $< 70\%$ ). Once reaching  
 547 larger RH ( $\sim 70\%$ ),  $f(\text{RH})$  begins to increase. However, for a small  $\eta$  (Fig. 11b), the  
 548 difference of the derivatives at 60% and 80% RH was small, meaning the curvature of  
 549 humidogram is much smaller.

550 A scatter plot of  $\eta$  and the mass percentage of nitrate is shown in Fig. 12, colored  
 551 by the mass percentage of sulfate. As can be seen,  $\eta$  is negatively correlated with the  
 552 mass percentage of nitrate. When the mass percentage of nitrate is below  $\sim 18\%$ , the  
 553 more nitrate, the smaller  $\eta$  is, which means the humidogram line becomes straighter  
 554 and the difference of the derivatives at lower and higher RHs becomes smaller. For a  
 555 mass percentage of nitrate higher than 18% (correspondingly, a lower sulfate mass  
 556 percentage),  $\eta$  is  $\sim 1.1$ , meaning the humidogram line is almost straight (as shown in  
 557 Fig. 11b) and aerosol scattering coefficient experiences a continuous and smooth  
 558 growth at almost the same rate with RH.

### 559 **3.7 Sensitivity of the direct radiative forcing of different aerosols to $f(\text{RH})$**

560 Direct radiative forcing of aerosols is quite sensitive to changes of relative  
 561 humidity. The impact of relative humidity on globally-averaged, direct radiative  
 562 forcing can be obtained by the following expression (Chylek and Wong, 1995):

$$563 \quad \Delta F_R(\text{RH}) = -[S_0/4][T_a^2(1 - A_c)][2(1 - R_s)^2\bar{\beta}(\text{RH})M\alpha_s f(\text{RH}) - 4R_s M\alpha_a] \quad (7)$$

564 where  $S_0$  is the solar constant,  $T_a$  is the transmittance of the atmosphere above the

565 aerosol layer,  $A_c$  is the fractional cloud amount,  $R_s$  is the albedo of the underlying  
 566 surface,  $\bar{\beta}(\text{RH})$  is the solar radiation scattered back to space at defined RH,  $f(\text{RH})$  is  
 567 the scattering enhancement factor,  $M$  is the column burden of aerosol (in  $\text{g m}^{-2}$ ),  $\alpha_s$  is  
 568 the mass scattering efficiency, and  $\alpha_a$  is the mass absorption efficiency.

569 In order to estimate the sensitivity of the forcing to different RHs for various  
 570 aerosol types (locally-polluted, northerly-polluted and dust-influenced aerosols), the  
 571 ratio of direct aerosol radiative forcing  $\Delta F_R$  at a defined RH to that at dry condition  
 572 was calculated:

$$\frac{\Delta F_R(\text{RH})}{\Delta F_R(\text{dry})} = \frac{(1 - R_s)^2 \bar{\beta}(\text{RH}) \alpha_s f(\text{RH}) - 2R_s \alpha_a}{(1 - R_s)^2 \bar{\beta}(\text{dry}) \alpha_s f(\text{dry}) - 2R_s \alpha_a} \quad (8)$$

573 Parameters used in Eq. (8) were  $R_s=0.15$ , and  $\alpha_a=0.3 \text{ m}^2 \text{ g}^{-1}$  (Wang et al., 2012; Hand  
 574 and Malm, 2007). The mass scattering efficiency  $\alpha_s$  is  $2.76 \text{ m}^2 \text{ g}^{-1}$ , which is derived  
 575 from the slope of a linear regression of the measured scattering coefficients and the  
 576 calculated  $\text{PM}_{10}$  mass concentrations based on TDMPS and APS measurement (see  
 577 Fig. 13); the high mass scattering efficiency is explained by the high ratio of  $\text{PM}_1$  to  
 578  $\text{PM}_{10}$  mass at this site (average 0.81). The average upscatter fraction  $\bar{\beta}$  was  
 579 calculated as  $\bar{\beta}=0.0817+1.8495b-2.9682b^2$  (Delene and Ogren, 2002). The sensitivity  
 580 of direct radiative forcing to RH for various aerosol types were shown in Fig. 14. As  
 581 is shown in the figure, the variation of  $\Delta F_R(\text{RH})/\Delta F_R(\text{dry})$  with RH was in accordance  
 582 with the variation of humidograms. The  $f(\text{RH})$  was the largest during the  
 583 northerly-polluted period, correspondingly, the effects of RH on aerosol radiative  
 584 forcing during this period was the largest. The same was true for the locally-polluted  
 585 period and the dust-influenced period. Since  $b$  decreases with increasing RH, this  
 586 correspondence also demonstrated the vital role  $f(\text{RH})$  played in direct forcing  
 587 enhancement. At 85% RH, the average ratio was 1.47, i.e. the direct radiative forcing  
 588 increased by 47% owing to the aerosol hygroscopicity.

589 Table 7 shows the mean influence of aerosol hygroscopicity on direct radiative  
 590 forcing in March at LinAn. The ratios  $\Delta F_R(\text{RH}_{\text{amb}})/\Delta F_R(\text{dry})$  for locally-polluted,  
 591 northerly-polluted and dust-influenced aerosols were calculated using the ambient  
 592 average RH ( $\text{RH}_{\text{amb}}=67\%$ ) in March at LinAn. The variables  $f(\text{RH}_{\text{amb}})$ ,  $b(\text{RH}_{\text{amb}})$ ,

593  $\bar{\beta}(\text{RH}_{\text{amb}})$  and  $\Delta F_{\text{R}}(\text{RH}_{\text{amb}})/\Delta F_{\text{R}}(\text{dry})$  were the averages of the linear interpolation  
594 results of  $f(\text{RH})$ ,  $b(\text{RH})$ ,  $\bar{\beta}(\text{RH})$  and  $\Delta F_{\text{R}}(\text{RH})/\Delta F_{\text{R}}(\text{dry})$  at 67% RH. The  
595  $\Delta F_{\text{R}}(\text{RH}_{\text{amb}})/\Delta F_{\text{R}}(\text{dry})$  ratios were 1.118, 1.195 and 1.105, respectively (see Table 7).  
596 That is to say, averagely, the direct radiative forcing of locally-polluted,  
597 northerly-polluted and dust-influenced aerosols increased by 11.8, 19.5 and 10.5% in  
598 March at LinAn.

599

#### 600 **4 Conclusions**

601 The influence of aerosol water uptake on particles' light scattering properties and  
602 direct radiative forcing have been investigated at LinAn, a regional atmospheric  
603 background station of Yangtze River Delta, China, using the scattering enhancement  
604 factor measurement system, together with AMS, MAAP and TDMPS providing the  
605 chemical composition and size distribution information. The average enhancement  
606 factors and mean standard deviations at 85% RH for scattering coefficient,  
607 backscattering coefficient and hemispheric backscatter fraction ( $f(85\%)$ ,  $f_{\text{b}}(85\%)$  and  
608  $f_{\beta}(85\%)$ ) were 1.58(0.12), 1.25(0.07) and 0.79(0.04), respectively. Slight wavelength  
609 dependence of  $f(85\%)$  was observed at higher  $f(\text{RH})$  values. Generally, the highest  
610 values of  $f(\text{RH})$  corresponded to aged aerosols with a small fraction of OM; while the  
611 lowest values corresponded to younger aerosols with a larger fraction of OM.  $f(\text{RH})$   
612 of aerosols with relatively low scattering coefficient was usually low with a large  
613 variation; while  $f(\text{RH})$  of aerosols with high scattering coefficients was relatively high  
614 with a small variation. Besides,  $\text{NO}_3^-$  plays an important role in determining the  
615 magnitude of  $f(\text{RH})$  at LinAn.

616 Humidograms measured at LinAn can be well described by the model  
617  $f(\text{RH})=c(1-\text{RH})^{-d}$  and model  $f(\text{RH})=1+a\text{RH}^b$ . Further investigation shows the shape  
618 of the humidogram is closely related to the mass percentage of nitrate. A steepness  
619 index  $\eta$  has been defined to quantitatively determine the steepness of humidograms.  
620 The more nitrate (or less sulfate), the smaller  $\eta$  is and the straighter the curve will be.  
621 In March, the average relative humidity ( $\text{RH}_{\text{amb}}$ ) was 67%. Consequently, the direct  
622 radiative forcing of locally-polluted, northerly-polluted and dust-influenced aerosols

623 increased by 11.8, 19.5 and 10.5%, respectively due to aerosol uptake water in March  
624 at LinAn. At 85% RH, the direct radiative forcing increased by as high as 47% due to  
625 the aerosol hygroscopicity. In conclusion, water plays an important role in aerosol  
626 scattering properties as well as the radiative forcing, and it should be paid high  
627 attention when comparing between remote sensing and in-situ measurements and  
628 calculating the climate forcing.

629

630

631 **Acknowledgments:** This work was supported by National Basic Research Program of  
632 China (2011CB403401), the National Natural Science Foundation of China  
633 (41475118, 41175113), China International Science and Technology Cooperation  
634 Project (2009DFA22800), CAMS Basis Research Project (2013Z007, 2013Y004),  
635 and the Meteorological Special Project of China (GYHY-200906038,  
636 GYHY201206037). This paper is partially supported by the CMA Innovation Team  
637 for Haze-fog Observation and Forecasts. The authors would also like to thank the  
638 LinAn observational station staff for their support. The authors would thank Dr. D.  
639 Covert of University of Washington Seattle Department of Atmospheric Sciences  
640 USA for useful discussions.

641

642

## 643 **References**

- 644 Ackerman, A. S., Kirkpatrick, M. P., Stevens, D. E., and Toon, O. B.: The impact of humidity above  
645 stratiform clouds on indirect aerosol climate forcing, *Nature*, 432, 1014-1017, 2004.
- 646 Adam, M., Putaud, J., Martins dos Santos, S., Dell'Acqua, A., and Gruening, C.: Aerosol hygroscopicity  
647 at a regional background site (Ispra) in Northern Italy, *Atmos. Chem. Phys*, 12, 5703-5717, 2012.
- 648 Anderson, T., Covert, D., Marshall, S., Laucks, M., Charlson, R., Waggoner, A., Ogren, J., Caldow, R.,  
649 Holm, R., and Quant, F.: Performance characteristics of a high-sensitivity, three-wavelength, total  
650 scatter/backscatter nephelometer, *J. Atmos. Ocean. Tech.*, 13, 967-986, 1996.
- 651 Anderson, T. L., and Ogren, J. A.: Determining aerosol radiative properties using the TSI 3563  
652 integrating nephelometer, *Aerosol Sci. Tech.*, 29, 57-69, 1998.
- 653 Berner, A., Lürzer, C., Pohl, F., Preining, O., and Wagner, P.: The size distribution of the urban aerosol in  
654 Vienna, *Sci. Total Environ.*, 13, 245-261, 1979.
- 655 Birmili, W., Stratmann, F., and Wiedensohler, A.: Design of a DMA-based size spectrometer for a large  
656 particle size range and stable operation, *J. Aerosol Sci.*, 30, 549-553, 1999.

657 Carrico, C. M., Rood, M. J., and Ogren, J. A.: Aerosol light scattering properties at Cape Grim, Tasmania,  
658 during the first Aerosol Characterization Experiment (ACE 1), *J. Geophys. Res.*, 103, 16565-16574,  
659 1998.

660 Carrico, C. M., Rood, M. J., Ogren, J. A., Neusüß, C., Wiedensohler, A., and Heintzenberg, J.: Aerosol  
661 Optical properties at Sagres, Portugal during ACE-2, *Tellus B*, 52, 694-715, 2000.

662 Carrico, C. M., Kus, P., Rood, M. J., Quinn, P. K., and Bates, T. S.: Mixtures of pollution, dust, sea salt,  
663 and volcanic aerosol during ACE-Asia: Radiative properties as a function of relative humidity, *J.*  
664 *Geophys. Res.*, 108, 8650, 10.1029/2003JD003405, 2003.

665 Charlson, R.J., Ahlquist, N., Selvidge, H., and MacCready Jr, P.: Monitoring of atmospheric aerosol  
666 parameters with the integrating nephelometer, *JAPCA J. Air Waste Ma.*, 19, 937-942, 1969.

667 Charlson, R. J., Schwartz, S., Hales, J., Cess, R. D., Coakley Jr, J. A., Hansen, J., and Hofmann, D.: Climate  
668 forcing by anthropogenic aerosols, *Science*, 255, 423-430, 1992.

669 Cheng, Y., Wiedensohler, A., Eichler, H., Heintzenberg, J., Tesche, M., Ansmann, A., Wendisch, M., Su,  
670 H., Althausen, D., and Herrmann, H.: Relative humidity dependence of aerosol optical properties  
671 and direct radiative forcing in the surface boundary layer at Xinken in Pearl River Delta of China: An  
672 observation based numerical study, *Atmos. Environ.*, 42, 6373-6397, 2008.

673 Chylek, P., and Wong, J.: Effect of absorbing aerosols on global radiation budget, *Geophys. Res. Lett.*,  
674 22, 929-931, 1995.

675 Covert, D. S., Charlson, R., and Ahlquist, N.: A study of the relationship of chemical composition and  
676 humidity to light scattering by aerosols, *J. Appl. Meteorol.*, 11, 968-976, 1972.

677 Day, D. E., and Malm, W. C.: Aerosol light scattering measurements as a function of relative humidity: a  
678 comparison between measurements made at three different sites, *Atmos. Environ.*, 35, 5169-5176,  
679 2001.

680 Delene, D. J., and Ogren, J. A.: Variability of aerosol optical properties at four North American surface  
681 monitoring sites, *J. Atmos. Sci.*, 59, 1135-1150, 2002.

682 Dick, W. D., Saxena, P., and McMurry, P. H.: Estimation of water uptake by organic compounds in  
683 submicron aerosols measured during the Southeastern Aerosol and Visibility Study, *J. Geophys.*  
684 *Res.-Atmos.*, 105, 1471-1479, 2000.

685 Doherty, S. J., Quinn, P. K., Jefferson, A., Carrico, C. M., Anderson, T. L., and Hegg, D.: A comparison and  
686 summary of aerosol optical properties as observed in situ from aircraft, ship, and land during  
687 ACE-Asia, *J. Geophys. Res.*, 110, D04201, doi: 10.1029/2004JD004964, 2005.

688 Engelhart, G., Hildebrandt, L., Kostenidou, E., Mihalopoulos, N., Donahue, N., and Pandis, S.: Water  
689 content of aged aerosol, *Atmos. Chem. Phys.*, 11, 911-920, 2011.

690 Fang, S. X., Zhou, L. X., Masarie, K. A., Xu, L., and Rella, C. W.: Study of atmospheric CH<sub>4</sub> mole fractions  
691 at three WMO/GAW stations in China, *J. Geophys. Res.-Atmos.*, 118, 4874-4886, 2013.

692 Fierz-Schmidhauser, R., Zieger, P., Gysel, M., Kammermann, L., DeCarlo, P., Baltensperger, U., and  
693 Weingartner, E.: Measured and predicted aerosol light scattering enhancement factors at the high  
694 alpine site Jungfrauoch, *Atmos. Chem. Phys.*, 10, 2319-2333, 2010.

695 Gasso, S., Hegg, D., Covert, D., Collins, D., Noone, K., Öström, E., Schmid, B., Russell, P., Livingston, J.,  
696 and Durkee, P.: Influence of humidity on the aerosol scattering coefficient and its effect on the  
697 upwelling radiance during ACE-2, *Tellus B*, 52, 546-567, 2000.

698 Hänel, G.: The properties of atmospheric aerosol particles as functions of the relative humidity at  
699 thermodynamic equilibrium with the surrounding moist air, *Adv. Geophys*, 19, 73-188, 1976.

700 Hand, J., and Malm, W.: Review of aerosol mass scattering efficiencies from ground-based

701 measurements since 1990, *J. Geophys. Res.-Atmos.*, 112, D16203, doi:10.1029/2007JD008484,  
702 2007.

703 Kim, J., Yoon, S.-C., Jefferson, A., and Kim, S.-W.: Aerosol hygroscopic properties during Asian dust,  
704 pollution, and biomass burning episodes at Gosan, Korea in April 2001, *Atmos. Environ.*, 40,  
705 1550-1560, 2006.

706 Koloutsou-Vakakis, S., Carrico, C., Kus, P., Rood, M., Li, Z., Shrestha, R., Ogren, J., Chow, J., and Watson,  
707 J.: Aerosol properties at a midlatitude Northern Hemisphere continental site, *J. Geophys. Res.*, 106,  
708 3019-3032, 2001.

709 Kotchenruther, R. A. and Hobbs, P. V.: Humidification factors of aerosols from biomass burning in  
710 Brazil, *J. Geophys. Res.*, 103, 32081-32089, doi: 10.1029/98jd00340, 1998.

711 Kotchenruther, R. A., Hobbs, P. V., and Hegg, D. A.: Humidification factors for atmospheric aerosols off  
712 the mid-Atlantic coast of the United States, *J. Geophys. Res.*, 104, 2239-2251, 1999.

713 Li-Jones, X., Maring, H. B., and Prospero, J. M.: Effect of relative humidity on light scattering by mineral  
714 dust aerosol as measured in the marine boundary layer over the tropical Atlantic Ocean, *J. Geophys.*  
715 *Res.*, 103, 31113-31121, 1998.

716 Liu, X., Zhang, Y., Jung, J., Gu, J., Li, Y., Guo, S., Chang, S.-Y., Yue, D., Lin, P., Kim, Y. J., Hu, M., Zeng, L.,  
717 and Zhu, T.: Research on the hygroscopic properties of aerosols by measurement and modeling  
718 during CAREBeijing-2006, *J. Geophys. Res.-Atmos.*, 114, D00G16, doi: 10.1029/2008JD010805, 2009.

719 Magi, B. I., and Hobbs, P. V.: Effects of humidity on aerosols in southern Africa during the biomass  
720 burning season, *J. Geophys. Res.-Atmos.* 108, 8504, doi:10.1029/2002JD002144, 2003.

721 Malm, W. C., and Day, D. E.: Optical properties of aerosols at Grand Canyon national park, *Atmos.*  
722 *Environ.*, 34, 3373-3391, 2000.

723 Malm, W. C., and Day, D. E.: Estimates of aerosol species scattering characteristics as a function of  
724 relative humidity, *Atmos. Environ.*, 35, 2845-2860, 2001.

725 Malm, W. C., Day, D. E., Kreidenweis, S. M., Collett, J. L., and Lee, T.: Humidity-dependent optical  
726 properties of fine particles during the Big Bend Regional Aerosol and Visibility Observational Study, *J.*  
727 *Geophys. Res.*, 108, 4279, doi:10.1029/2002JD002998, 2003.

728 Malm, W. C., Day, D. E., Kreidenweis, S. M., Collett, J. L., Carrico, C., McMeeking, G., and Lee, T.:  
729 Hygroscopic properties of an organic-laden aerosol, *Atmos. Environ.*, 39, 4969-4982, 2005.

730 Meng, Z. Y., Jia, X. F., Zhang, R. J., Yu, X. M., and Ma, Q. L.: Characteristics of PM<sub>2.5</sub> at Lin'an Regional  
731 Background Station in the Yangtze River Delta Region, *J. Appl. Meteorol. Sci.*, 23, 424-432, 2012.

732 Morgan, W., Allan, J., Bower, K., Esselborn, M., Harris, B., Henzing, J., Highwood, E., Kiendler-Scharr, A.,  
733 McMeeking, G., and Mensah, A.: Enhancement of the aerosol direct radiative effect by  
734 semi-volatile aerosol components: airborne measurements in North-Western Europe, *Atmos. Chem.*  
735 *Phys.*, 10, 8151-8171, 2010.

736 Müller T., Laborde M., Kassell G., and Wiedensohler A., Design and performance of a three wavelength  
737 LED-based total scatter and backscatter integrating nephelometer, *Atmos. Meas. Tech.*, 4(6), 1291-  
738 1303, doi:10.5194/amt-4-1291-2011, 2011.

739 Pan, L., Che, H., Geng, F., Xia, X., Wang, Y., Zhu, C., Chen, M., Gao, W., and Guo, J.: Aerosol optical  
740 properties based on ground measurements over the Chinese Yangtze Delta Region, *Atmos. Environ.*,  
741 44, 2587-2596, 2010.

742 Pan, X. L., Yan, P., Tang, J., Ma, J., Wang, Z., Gbaguidi, A., and Sun, Y.: Observational study of influence  
743 of aerosol hygroscopic growth on scattering coefficient over rural area near Beijing mega-city,  
744 *Atmos. Chem. Phys.*, 9, 7519-7530, 2009.



745 Pilinis, C., Seinfeld, J. H., and Grosjean, D.: Water content of atmospheric aerosols, *Atmos. Environ.*, 23,  
746 1601-1606, 1989.

747 Pilinis, C., Pandis, S. N., and Seinfeld, J. H.: Sensitivity of direct climate forcing by atmospheric aerosols  
748 to aerosol size and composition, *J. Geophys. Res.*, 100, 18739-18754, 1995.

749 Qi, H., Lin, W., Xu, X., Yu, X., and Ma, Q.: Significant downward trend of SO<sub>2</sub> observed from 2005 to  
750 2010 at a background station in the Yangtze Delta region, China, *Sci. China Ser. B*, 55, 1451-1458,  
751 2012.

752 Quinn, P., Marshall, S., Bates, T., Covert, D., and Kapustin, V.: Comparison of measured and calculated  
753 aerosol properties relevant to the direct radiative forcing of tropospheric sulfate aerosol on climate,  
754 *J. Geophys. Res.*, 100, 8977-8991, 1995.

755 Quinn, P. K., Bates, T. S., Baynard, T., Clarke, A. D., Onasch, T. B., Wang, W., Rood, M. J., Andrews, E.,  
756 Allan, J., Carrico, C. M., Coffman, D., and Worsnop, D.: Impact of particulate organic matter on the  
757 relative humidity dependence of light scattering: A simplified parameterization, *Geophys. Res. Lett.*,  
758 32, L22809, doi: 10.1029/2005gl024322, 2005.

759 Randles, C., Russell, L., and Ramaswamy, V.: Hygroscopic and optical properties of organic sea salt  
760 aerosol and consequences for climate forcing, *Geophys. Res. Lett.*, 31, L16108,  
761 doi:10.1029/2004GL020628, 2004.

762 Shen, X., Sun, J., Zhang, Y., Wehner, B., Nowak, A., Tuch, T., Zhang, X., Wang, T., Zhou, H., and Zhang, X.:  
763 First long-term study of particle number size distributions and new particle formation events of  
764 regional aerosol in the North China Plain, *Atmos. Chem. Phys.*, 11, 1565-1580,  
765 doi:10.5194/acp-11-1565-2011, 2011.

766 Shi, Y., Chen, J., Hu, D., Wang, L., Yang, X., and Wang, X.: Airborne submicron particulate (PM<sub>1</sub>)  
767 pollution in Shanghai, China: Chemical variability, formation/dissociation of associated  
768 semi-volatile components and the impacts on visibility, *Sci. Total Environ.*, 473, 199-206, 2014.

769 Shi, Z., Zhang, D., Hayashi, M., Ogata, H., Ji, H., and Fujiie, W.: Influences of sulfate and nitrate on the  
770 hygroscopic behaviour of coarse dust particles, *Atmos. Environ.*, 42, 822-827, 2008.

771 Sjogren, S., Gysel, M., Weingartner, E., Baltensperger, U., Cubison, M., Coe, H., Zardini, A., Marcolli, C.,  
772 Krieger, U., and Peter, T.: Hygroscopic growth and water uptake kinetics of two-phase aerosol  
773 particles consisting of ammonium sulfate, adipic and humic acid mixtures, *J. Aerosol Sci.*, 38,  
774 157-171, 2007.

775 Sullivan, R., Moore, M., Petters, M., Kreidenweis, S., Roberts, G., and Prather, K.: Effect of chemical  
776 mixing state on the hygroscopicity and cloud nucleation properties of calcium mineral dust particles,  
777 *Atmos. Chem. Phys.*, 9, 3303-3316, 2009.

778 Sun, J., Zhang, Q., Canagaratna, M. R., Zhang, Y., Ng, N. L., Sun, Y., Jayne, J. T., Zhang, X., Zhang, X., and  
779 Worsnop, D. R.: Highly time- and size-resolved characterization of submicron aerosol particles in  
780 Beijing using an Aerodyne Aerosol Mass Spectrometer, *Atmos. Environ.*, 44, 131-140, 2010.

781 Sun, Y., Wang, Z., Dong, H., Yang, T., Li, J., Pan, X., Chen, P., and Jayne, J. T.: Characterization of summer  
782 organic and inorganic aerosols in Beijing, China with an Aerosol Chemical Speciation Monitor,  
783 *Atmos. Environ.*, 51, 250-259, 2012.

784 Tang, I. N.: Chemical and size effects of hygroscopic aerosols on light scattering coefficients, *J. Geophys.*  
785 *Res.-Atmos*, 101, 19245-19250, 1996.

786 Tobo, Y., Zhang, D., Matsuki, A., and Iwasaka, Y.: Asian dust particles converted into aqueous droplets  
787 under remote marine atmospheric conditions, *P. Natl. Acad. Sci. USA*, 107, 17905-17910, 2010.

788 Tuch, T. M., Haudek, A., Müller, T., Nowak, A., Wex, H., and Wiedensohler, A.: Design and performance

789 of an automatic regenerating adsorption aerosol dryer for continuous operation at monitoring sites,  
790 *Atmos. Meas. Tech.*, 2, 417–422, doi:10.5194/amt-2-417-2009, 2009.

791 Wang, Y., Zhang, X., and Draxler, R. R.: TrajStat: GIS-based software that uses various trajectory  
792 statistical analysis methods to identify potential sources from long-term air pollution measurement  
793 data, *Environ. Modell. Softw.*, 24, 938–939, 2009.

794 Wang, J. and Martin, S. T.: Satellite characterization of urban aerosols: Importance of including  
795 hygroscopicity and mixing state in the retrieval algorithms, *J. Geophys. Res.-Atmos.*, 112, D17203,  
796 doi:10.1029/2006JD008078, 2007.

797 Wang, M. X., Ding, X., Fu, X., He, Q., Wang, S., Bernard, F., Zhao, X., and Wu, D.: Aerosol scattering  
798 coefficients and major chemical compositions of fine particles observed at a rural site in the central  
799 Pearl River Delta, South China, *J. Environ. Sci.*, 24, 72–77, 2012.

800 Wang, L. P., Zhang, B. H., and Zhang, X. W.: Main weather processes in March and April, 2013, *Weather*  
801 *Forecast Rev.*, 5, 1–7, 2013.

802 Weingartner, E., Baltensperger, U., and Burtscher, H.: Growth and structural change of combustion  
803 aerosols at high relative humidity, *Environ. Sci. Technol.*, 29, 2982–2986, 1995.

804 Wiscombe, W., and Grams, G.: The backscattered fraction in two-stream approximations, *J. Atmos. Sci.*,  
805 33, 2440–2451, 1976.

806 Xu, J., Bergin, M., Yu, X., Liu, G., Zhao, J., Carrico, C., and Baumann, K.: Measurement of aerosol  
807 chemical, physical and radiative properties in the Yangtze delta region of China, *Atmos. Environ.*, 36,  
808 161–173, 2002.

809 Xu, X., Lin, W., Wang, T., Yan, P., Tang, J., Meng, Z., and Wang, Y.: Long-term trend of surface ozone at a  
810 regional background station in eastern China 1991–2006: enhanced variability, *Atmos. Chem. Phys.*,  
811 8, 2595–2607, doi:10.5194/acp-8-2595-2008, 2008.

812 Yan, P., Zhang, Y. M., Yang, D. Z., Tang, J., Yu, X. L., Cheng, H. B., and Yu, X. M.: The characteristic of  
813 aerosol ionic size distributions at Lin'an in summer of 2003, *Acta Meteor. Sin.*, 63, 980–987, 2005.

814 Yan, P., Pan, X., Tang, J., Zhou, X., Zhang, R., and Zeng, L.: Hygroscopic growth of aerosol scattering  
815 coefficient: A comparative analysis between urban and suburban sites at winter in Beijing,  
816 *Particuology*, 7, 52–60, 2009.

817 Zhang, B. and Sun, J.: Analysis of the March 2013 atmospheric circulation and Weather, *Meteor. Mon.*,  
818 39, 794–800, 2013.

819 Zhang, Y. Y., Zuo, L. F., Ren, X. C., and Cui, J.: Research of the aerosol scattering properties based on  
820 evaporation duct, *Ship Electron. Eng.*, 32, 12–14, 2012.

821 Zhejiang Environmental Protection Bureau (ZEPB), 1999, Annual Report on the State of the  
822 Environment of Zhejiang Province, Zhejiang Environmental Protection Bureau, Hangzhou, 1999.

823 Zhejiang Environmental Protection Bureau (ZEPB), 2006, Annual Report on the State of the  
824 Environment of Zhejiang Province, Zhejiang Environmental Protection Bureau, Hangzhou, 21 pp.,  
825 2006.

826 Zhejiang Environmental Protection Bureau (ZEPB), 2012, Annual Report on the State of the  
827 Environment of Zhejiang Province, Zhejiang Environmental Protection Bureau, Hangzhou, 29 pp.,  
828 2012.

829 Zhejiang Environmental Protection Bureau (ZEPB), 2013, Annual Report on the State of the  
830 Environment of Zhejiang Province, Zhejiang Environmental Protection Bureau, Hangzhou, 33 pp.,  
831 2013.

832 Zieger, P., Fierz-Schmidhauser, R., Gysel, M., Ström, J., Henne, S., Yttri, K. E., Baltensperger, U., and

833 Weingartner, E.: Effects of relative humidity on aerosol light scattering in the Arctic, *Atmos. Chem.*  
834 *Phys.*, 10, 3875-3890, doi:10.5194/acp-10-3875-2010, 2010.

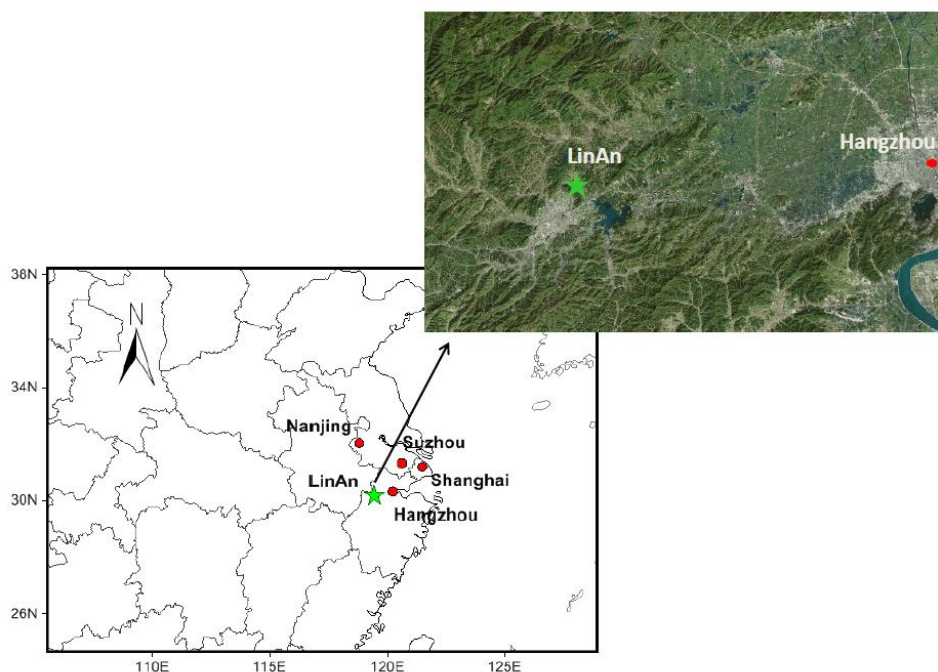
835 Zieger, P., Weingartner, E., Henzing, J., Moerman, M., Leeuw, G. d., Mikkilä, J., Ehn, M., Petäjä, T.,  
836 Clémer, K., and Roozendaal, M. v.: Comparison of ambient aerosol extinction coefficients obtained  
837 from in-situ, MAX-DOAS and LIDAR measurements at Cabauw, *Atmos. Chem. Phys.*, 11, 2603-2624,  
838 doi:10.5194/acp-11-2603-2011, 2011.

839 Zieger, P., Kienast-Sjögren, E., Starace, M., Bismarck, J. v., Bukowiecki, N., Baltensperger, U., Wienhold,  
840 F., Peter, T., Ruhtz, T., and Collaud Coen, M.: Spatial variation of aerosol optical properties around  
841 the high-alpine site Jungfraujoch (3580 m asl), *Atmos. Chem. Phys.*, 12, 7231-7249,  
842 doi:10.5194/acp-12-7231-2012, 2012.

843 Zieger, P., Fierz-Schmidhauser, R., Weingartner, E., and Baltensperger, U.: Effects of relative humidity  
844 on aerosol light scattering: results from different European sites, *Atmos. Chem. Phys.*, 13,  
845 10609-10631, doi:10.5194/acp-13-10609-2013, 2013.

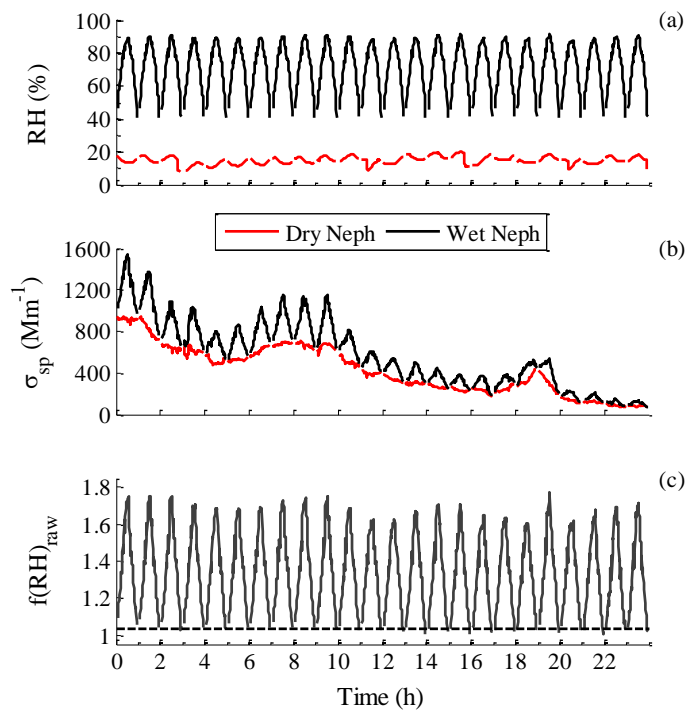
846 Zieger, P., Fierz-Schmidhauser, R., Poulain, L., Müller, T., Birmili, W., Spindler, G., Wiedensohler, A.,  
847 Baltensperger, U., and Weingartner, E.: Influence of water uptake on the aerosol particle light  
848 scattering coefficients of the Central European aerosol, *Tellus B*, 66, 22716,  
849 doi:10.3402/tellusb.v66.22716, 2014.

850



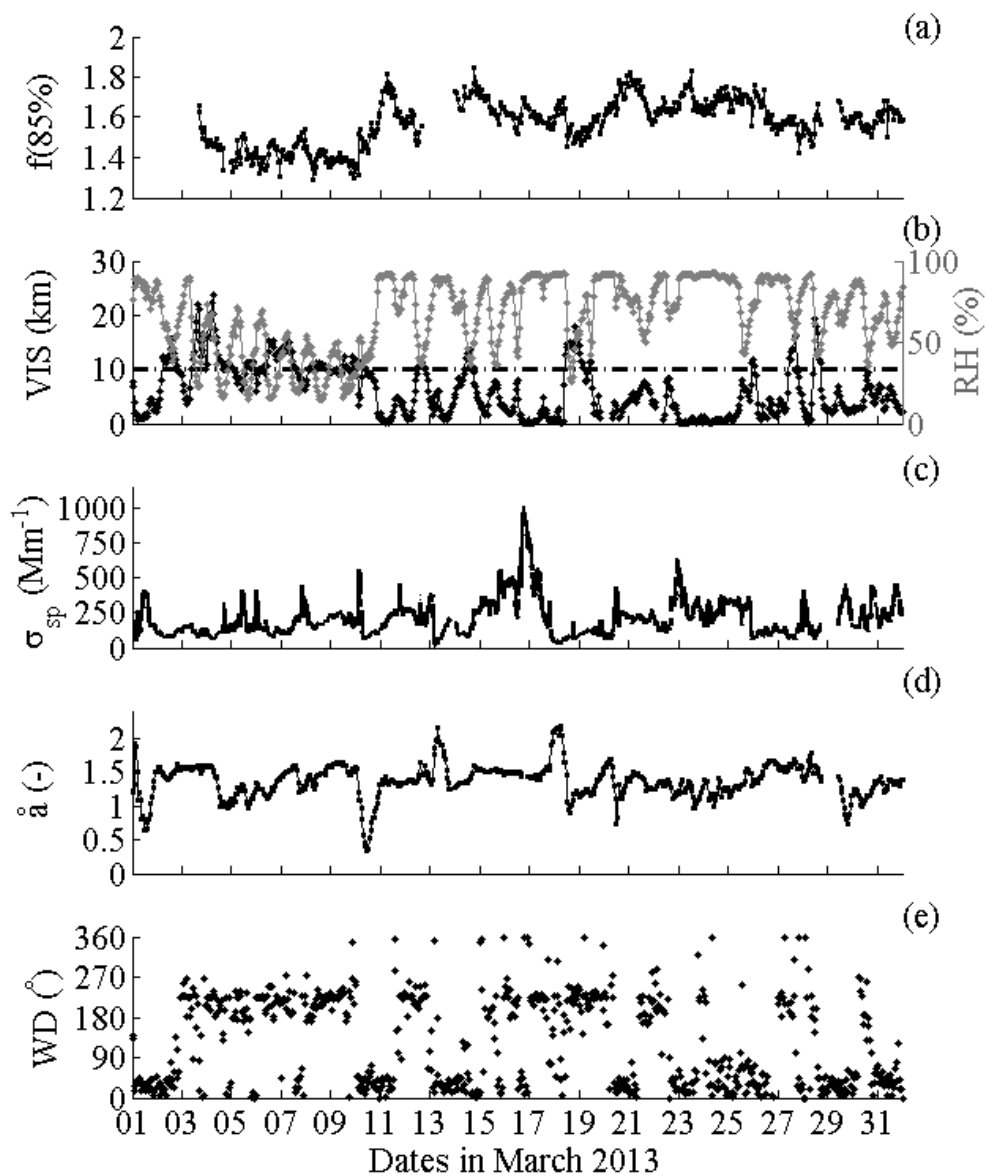
851

852 Fig. 1 Location of LinAn station (green star) and the main cities in the Yangtze River  
853 Delta (red dots) in the lower left panel. The upper right panel is the topography of the  
854 surrounding area.



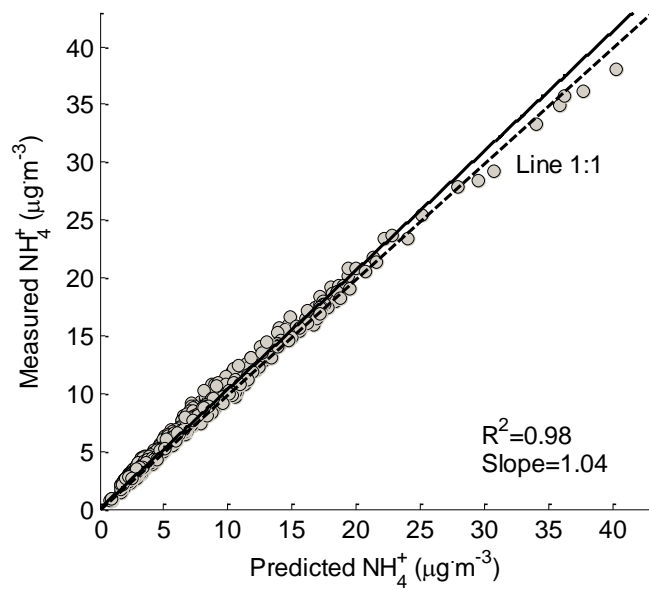
855

856 Fig. 2 Example of recorded data on 17 March 2013 (a) Relative humidity inside  
 857 DryNeph (red line) and WetNeph (black line); (b) Aerosol scattering coefficients  
 858 measured by DryNeph (red line) and WetNeph (black line) at 550nm wavelength; (c)  
 859 Raw scattering enhancement factor  $f(\text{RH}, 550\text{nm})_{\text{raw}}$  without normalization, the black  
 860 dash line was  $f(\text{RH})_{\text{raw}}=1.03$ .



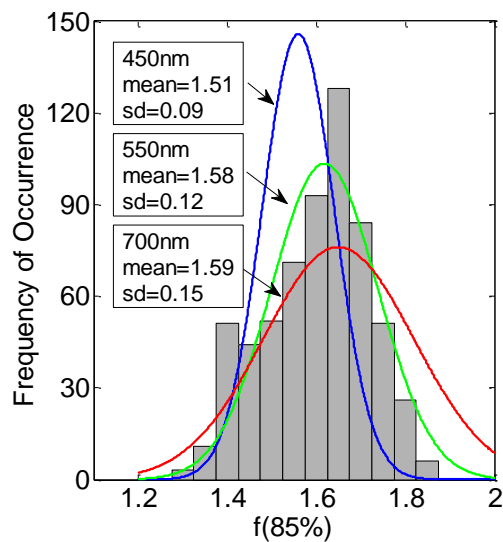
861

862 Fig. 3 Time series of measured and derived aerosol variables, as well as the ambient  
 863 RH and visibility. (a) scattering enhancement factor  $f(85\%)$  at 550 nm wavelength; (b)  
 864 visibility (VIS) and relative humidity (RH) at ambient conditions, the dashed line  
 865 represents  $VIS=10$  km; (c) aerosol scattering coefficient of DryNeph at 550 nm  
 866 wavelength; (d) Ångström exponent  $\hat{a}$  (e) wind direction (WD), indicating prevailing  
 867 wind directions during observation period was mainly northeasterly (NE) and  
 868 southwesterly (SW).



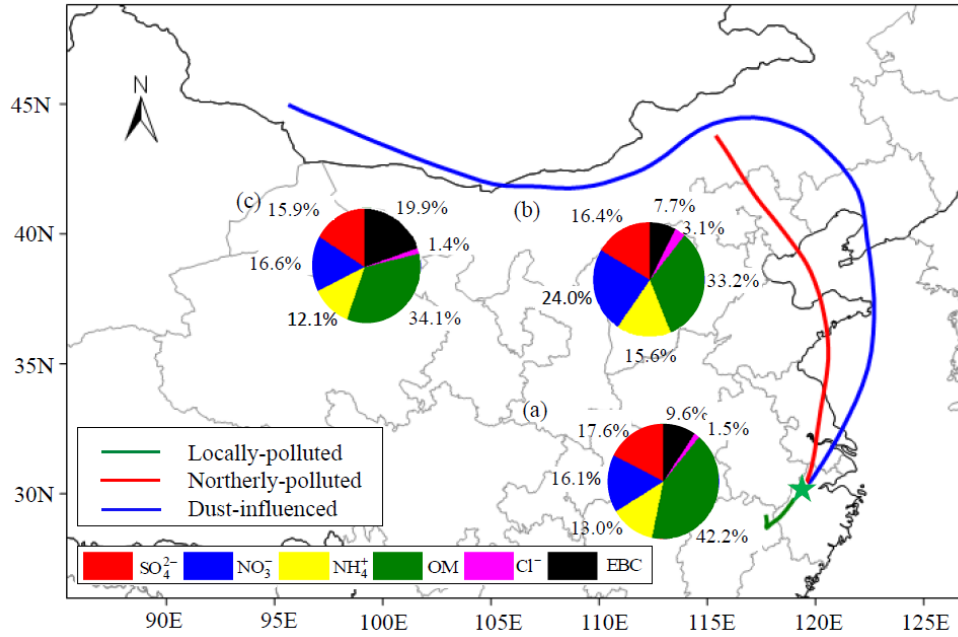
869

870 Fig. 4 Measured and predicted mass concentration of ammonium. The predicted mass  
 871 concentration of ammonium ( $\text{NH}_4^+$  predicted) is calculated by Eq. (4). The solid black  
 872 line represents the linear least square regression.



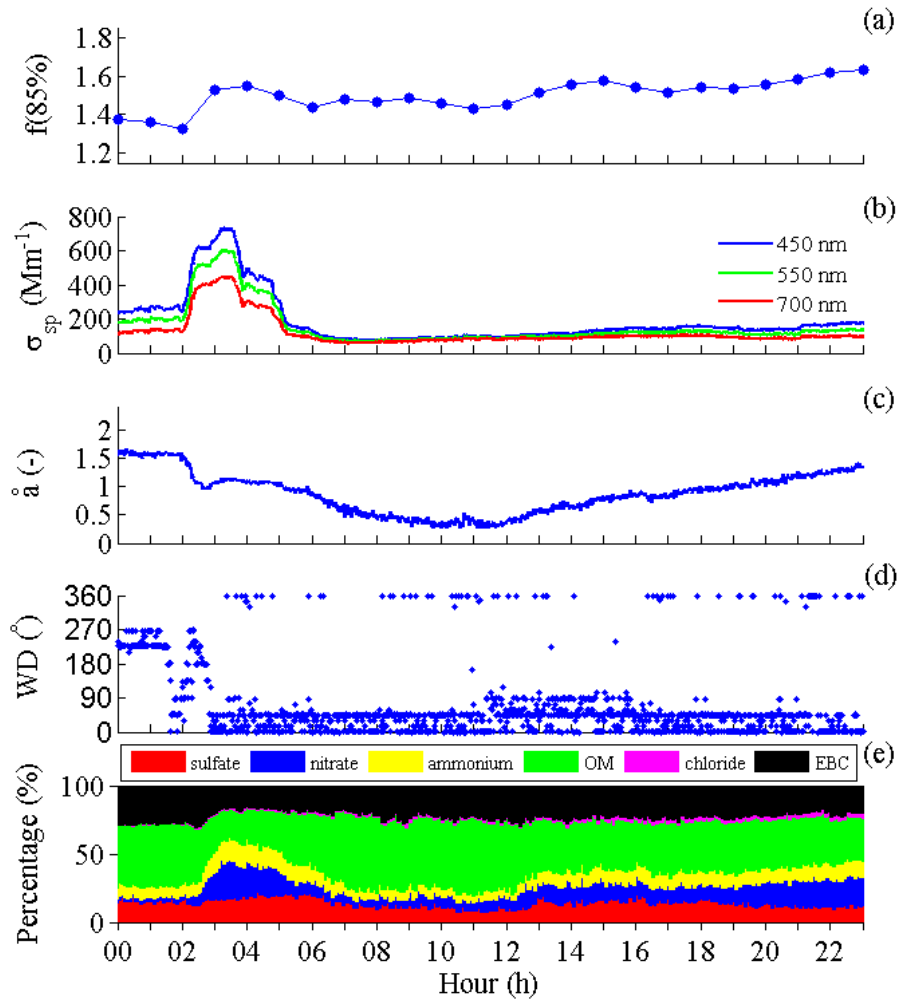
873

874 Fig. 5 Histograms of  $f(85\%, 550 \text{ nm})$  overlaid with the Gaussian curves based on the  
 875 statistics for  $f(85\%, 450 \text{ nm})$ ,  $f(85\%, 550 \text{ nm})$  and  $f(85\%, 700 \text{ nm})$ .



876

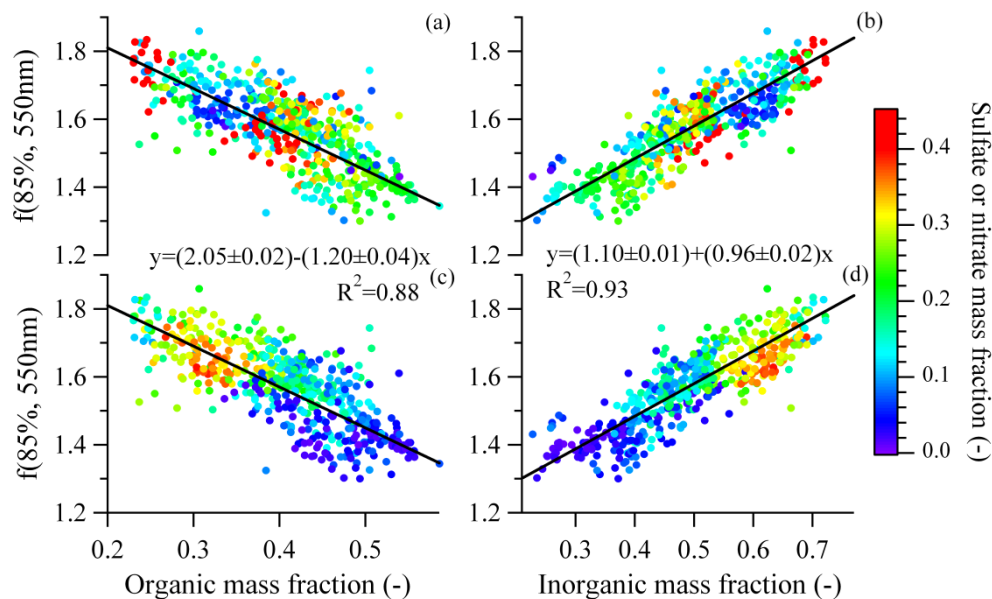
877 Fig. 6 72h back trajectories of locally-polluted period, northerly-polluted period and  
 878 dust-influenced period, together with the mean mass fraction of submicron chemical  
 879 compositions (SO<sub>4</sub><sup>2-</sup>, NO<sub>3</sub><sup>-</sup>, NH<sub>4</sub><sup>+</sup>, OM and Cl<sup>-</sup>) measured by AMS and EBC in PM<sub>10</sub>  
 880 measured by MAAP. The pie chart (a), (b) and (c) were for locally-polluted,  
 881 northerly-polluted and dust-influenced periods, respectively.



882

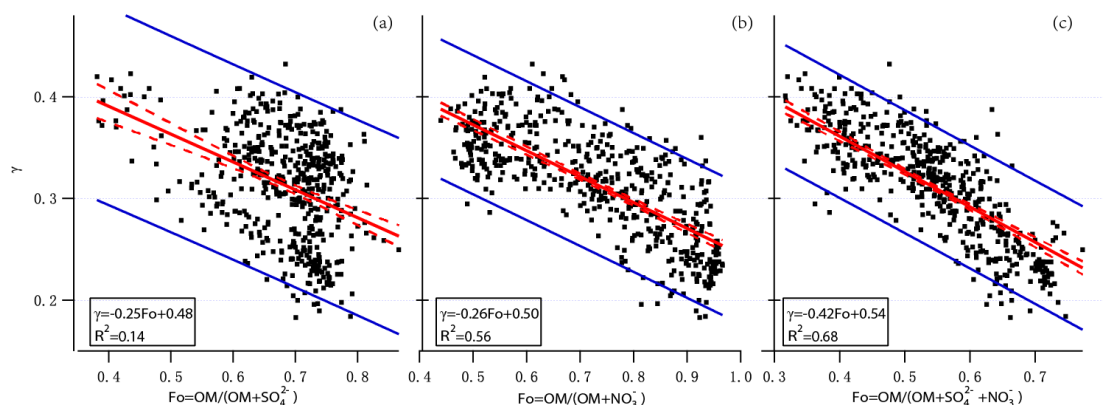
883 Fig. 7 Parameters in episode influenced by dust on 10 March 2013 at LinAn (a)  
 884 scattering enhancement factor  $f(85\%)$  at 550nm wavelength; (b) scattering  
 885 coefficients at 450nm, 550nm and 700nm wavelengths; (c) Ångström exponent  $\tilde{a}$  (d)  
 886 wind direction; (e) mass percentages of chemical species measured by AMS and  
 887 MAAP.





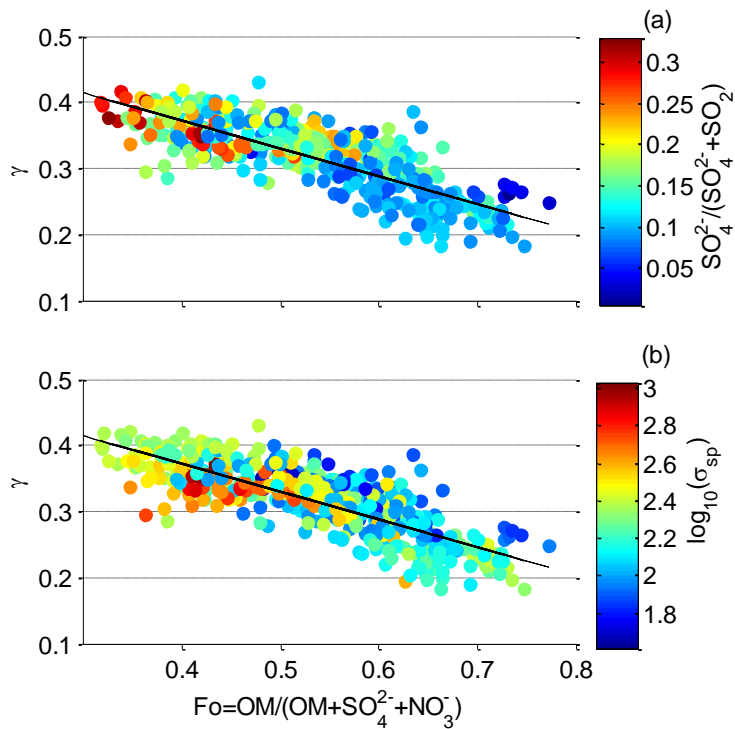
888

889 Fig. 8 Scattering enhancement factor  $f(85\%, 550\text{nm})$  vs. organic mass fraction and  
 890 inorganic mass fraction determined from AMS and MAAP: (a) (b)  $f(85\%, 550\text{nm})$  vs.  
 891 organic mass and inorganic mass fraction colored by sulfate mass fraction,  
 892 respectively; (c) (d)  $f(85\%, 550\text{nm})$  vs. organic mass fraction and inorganic mass  
 893 fraction colored by nitrate mass fraction, respectively. The solid black line represent a  
 894 bivariate linear regression including the uncertainty of  $f(85\%, 550\text{nm})$  and the  
 895 standard deviation of chemical compositions.



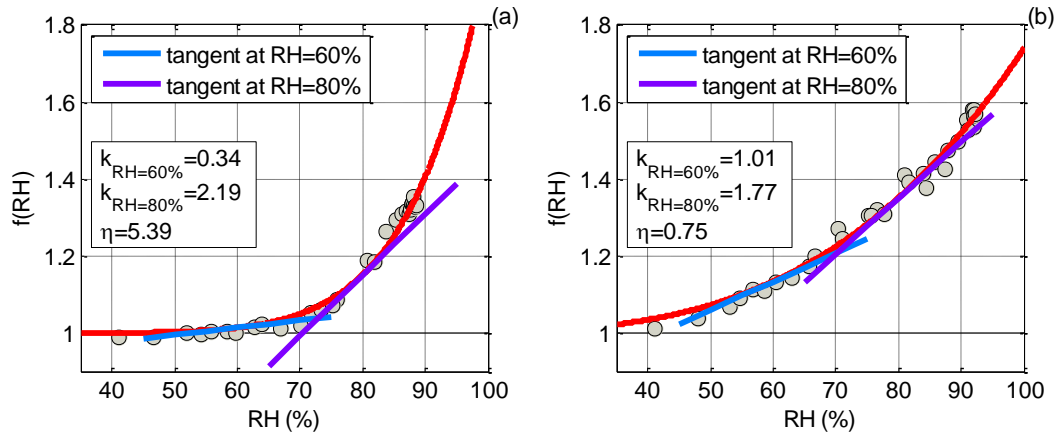
896

897 Fig. 9 scatter plots of  $\gamma$  versus  $F_o$  (a)  $F_o = \text{OM} / (\text{OM} + \text{SO}_4^{2-})$ , (b)  $F_o = \text{OM} / (\text{OM} + \text{NO}_3^-)$   
 898 and (c)  $F_o = \text{OM} / (\text{OM} + \text{SO}_4^{2-} + \text{NO}_3^-)$ . Solid red lines represent the linear fit, dashed red  
 899 lines show the 95% confidence level for the fit, and solid blue lines show the 95%  
 900 prediction bands.



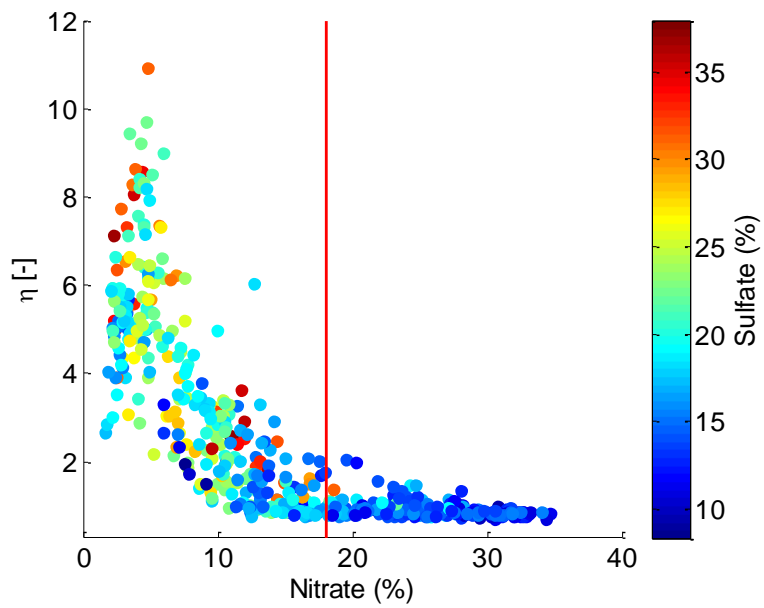
901

902 Fig. 10  $\gamma$  versus  $Fo=OM/(OM+SO_4^{2-}+NO_3^-)$  colored by (a)  $SO_4^{2-}/(SO_4^{2-}+SO_2)$  molar  
 903 ratio and (b)  $\log_{10}(\sigma_{sp})$ .



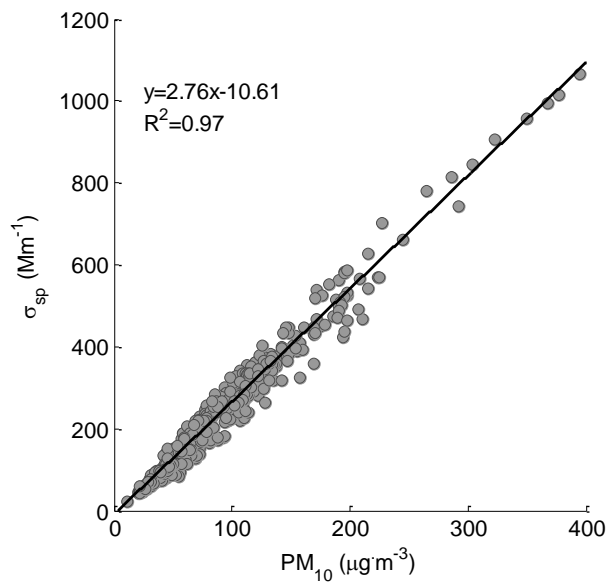
904

905 Fig. 11 Two distinct examples showing different growth patterns and the  
 906 corresponding  $\eta$  (a) 2013.03.08 18h  $f(RH)$  increased slowly at low RH (usually <70%)  
 907 and then increase more steeply, thus  $\eta$  is big; (b) 2013.03.10 21h  $f(RH)$  increased with  
 908 nearly constant speed and  $\eta$  is small.  $k_{RH=60\%}$  and  $k_{RH=80\%}$  represent the derivatives at  
 909 60% and 80% RH, respectively.  $f(RH)$  were at 550nm wavelength.



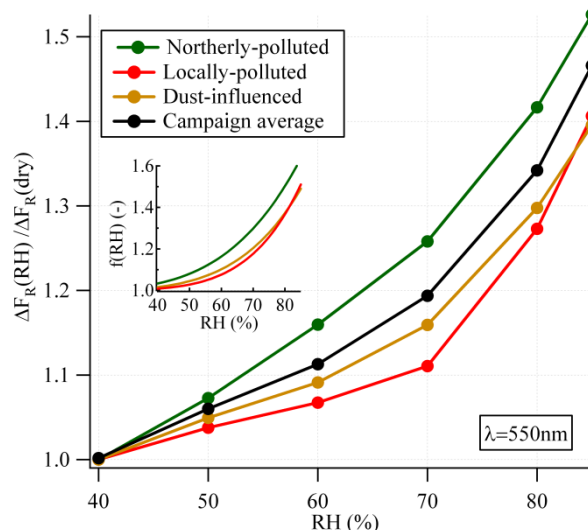
910

911 Fig. 12 Scatter plot of  $\eta$  and the mass percentage of nitrate, colored by the mass  
 912 percentage of sulfate.



913

914 Fig. 13 Linear regression of scattering coefficients ( $\sigma_{sp}$ ) at 550nm wavelength and  
 915  $PM_{10}$  mass concentration.



916

917 Fig. 14 Influence of relative humidity (RH) on direct radiative forcing for the entire  
 918 campaign (black line), as well as for the northerly-polluted, locally-polluted and  
 919 dust-polluted periods, measured by the ratio of radiative forcing at a certain RH to  
 920 that at dry conditions. The small inlay shows the fitting curves of  $f(\text{RH})$  for  
 921 northerly-polluted, locally-polluted and dust-polluted periods, respectively, using  
 922 fitting parameters in Table 6. All the parameters were measured at 550nm wavelength.

923

924 Table 1 Averaged enhancement factors and mean standard deviations for scattering  
 925 coefficient, backscattering coefficient and hemispheric backscatter fraction at  
 926 different RHs (550nm wavelength).

RH(%)	$f(\text{RH})$	$f_b(\text{RH})$	$f_\beta(\text{RH})$
50	1.07(0.04)	1.04(0.02)	0.96(0.02)
60	1.14(0.08)	1.06(0.04)	0.93(0.04)
70	1.24(0.11)	1.10(0.05)	0.89(0.05)
80	1.43(0.12)	1.18(0.07)	0.83(0.05)
85	1.58(0.12)	1.25(0.07)	0.79(0.04)

927

928 Table 2 Summary of mass concentrations ( $\mu\text{g}\cdot\text{m}^{-3}$ ) of aerosol species measured by  
 929 AMS as well as MAAP(\*) (SD: standard deviation)

Mean	SD	Minimum	Maximum
------	----	---------	---------

Sulfate	8.1	4.1	0.1	26.1
Nitrate	9.8	12.1	0.2	79.2
Ammonium	6.9	5.5	0.5	42.8
Chloride	1.1	2.0	0.002	22.9
OM	17.7	11.1	2.8	93.9
EBC*	4.1	2.8	0.7	25.3

930 \* EBC was measured by MAAP in PM<sub>10</sub>.

931

932 Table 3 Statistical values of f(85%) at 450 nm, 550 nm and 700 nm wavelengths (SD:  
933 standard deviation; prctl: percentile)

$\lambda$	mean	SD	90th prctl.	75th prctl.	median	25th prctl.	10th prctl.
450 nm	1.51	0.09	1.63	1.58	1.53	1.47	1.39
550 nm	1.58	0.12	1.72	1.65	1.59	1.49	1.40
700 nm	1.59	0.15	1.77	1.70	1.62	1.46	1.36

934

935 Table 4 Average enhancement factors and mean standard deviations for scattering  
936 coefficient, backscattering coefficient and hemispheric backscatter fraction in various  
937 observation episodes (550nm wavelength).

	Locally-polluted	Northerly-polluted	Dust-influenced
f(80%)	1.36(0.11)	1.50(0.09)	1.37(0.05)
f <sub>b</sub> (80%)	1.15(0.06)	1.21(0.06)	1.15(0.03)
f <sub><math>\beta</math></sub> (80%)	0.85(0.04)	0.81(0.03)	0.84(0.03)
f(85%)	1.52(0.10)	1.64(0.09)	1.48(0.05)
f <sub>b</sub> (85%)	1.21(0.06)	1.28(0.06)	1.19(0.04)
f <sub><math>\beta</math></sub> (85%)	0.80(0.02)	0.78(0.02)	0.81(0.03)
N	295	303	14

938

939 Table 5 Curve-fitting parameters of f(RH) at 550nm wavelength for various aerosol  
940 types in terms of equation  $f(\text{RH})=c(1-\text{RH})^{-g}$ .

c	g	Reference
---	---	-----------

Locally-polluted	0.85±0.08	0.29±0.04	
Northerly-polluted	0.93±0.07	0.28±0.03	This work
Dust-influenced	0.87±0.05	0.27±0.02	
Continental	0.9±0.1	-	Zieger et al. (2014)
Arctic <sup>a</sup>	1	0.58±0.09	Zieger et al. (2010)
Marine	0.99	0.54	
Polluted	0.59	0.77	Carrico et al. (2003)
Dust	0.60	0.61	
Polluted Marine	1	0.57±0.06	
Dust	1	0.23±0.05	Gass ó et al. (2000)
Clean Marine1 <sup>b</sup>	1	0.69±0.06	
Clean Marine2 <sup>c</sup>	1	0.73±0.07	

941 a fitting results for aerosol samples with RH>75%

942 b fitting results for aerosol samples with RH>60%

943 c fitting results for aerosol samples with RH>80%

944

945 Table 6 Curve-fitting parameters of f(RH) at 550nm wavelength for various aerosol

946 types in terms of Eq. (5).

	a	b	Reference
Locally-polluted	1.24±0.29	5.46±1.90	
Northerly-polluted	1.20±0.21	3.90±1.27	This work
Dust-influenced	1.02±0.19	4.51±0.80	
Clean	1.20±0.06	6.07±0.27	
Polluted	2.30±0.03	6.27±0.10	Pan et al. (2009)
Dust	0.64±0.04	5.17±0.40	
Urban	2.06	3.60	
Mixed	3.26	3.85	Liu et al. (2007)
Marine	4.92	5.04	

947

948 Table 7 Estimated effects of aerosol hygroscopic growth on direct radiative forcing by  
 949 locally-polluted, northerly-polluted and dust-influenced aerosols at LinAn, measured  
 950 by the ratio ( $\Delta F_R(\text{RH}_{\text{amb}})/\Delta F_R(\text{dry})$ ) of direct aerosol radiative forcing at the ambient  
 951 average relative humidity ( $\text{RH}_{\text{amb}}=67\%$ ) for the entire campaign to that in dry  
 952 condition. All the parameters were measured at 550nm wavelength.

	$f(\text{RH}_{\text{amb}})$	$b(\text{dry})$	$\bar{\beta}(\text{dry})$	$b(\text{RH}_{\text{amb}})$	$\bar{\beta}(\text{RH}_{\text{amb}})$	$\Delta F_R(\text{RH}_{\text{amb}})/\Delta F_R(\text{dry})$
Entire campaign	1.21	0.126	0.268	0.115	0.255	1.157
Locally-polluted	1.17	0.131	0.274	0.123	0.263	1.118
Northerly-polluted	1.26	0.121	0.262	0.106	0.243	1.195
Dust-influenced	1.15	0.146	0.289	0.132	0.274	1.105

953